

# Detection of Linear Features in SAR Images: Application to Road Network Extraction

Florence Tupin, Henri Maître, Jean-François Mangin, Jean-Marie Nicolas, and Eugène Pechersky

**Abstract**—We propose a two-step algorithm for almost unsupervised detection of linear structures, in particular, main axes in road networks, as seen in synthetic aperture radar (SAR) images. The first step is local and is used to extract linear features from the speckle radar image, which are treated as road-segment candidates. We present two local line detectors as well as a method for fusing information from these detectors. In the second global step, we identify the real roads among the segment candidates by defining a Markov random field (MRF) on a set of segments, which introduces contextual knowledge about the shape of road objects. The influence of the parameters on the road detection is studied and results are presented for various real radar images.

**Index Terms**—Markov random fields (MRF's), road detection, SAR images, statistical properties.

## NOMENCLATURE

$L$	Number of looks of the radar image.
$A_s$	Amplitude of pixel $s$ .
$n_i$	Number of pixels in region $i$ .
$\mu_i$	Empirical mean of region $i$ .
$\gamma_i$	Empirical variation coefficient of region $i$ .
$\langle I_i \rangle$	Exact mean-reflected intensity of region $i$ .
$c_{ij}, \bar{c}_{ij}$	Exact and empirical contrasts between regions $i$ and $j$ .
$r_{ij}$	Ratio edge detector response between regions $i$ and $j$ .
$r$	Ratio line detector (D1) response.
$\rho_{ij}$	Cross-correlation edge detector response between regions $i$ and $j$ .
$\rho$	Cross-correlation line detector (D2) response.
$x_{\min}$	Decision threshold for variable $x$ .
$f_x(t p_1, \dots, p_k)$	Probability-density function (pdf) of a random variable $x$ for value $t$ and parameter values $p_1, \dots, p_k$ .
$\Phi_x(t p_1, \dots, p_k)$	Cumulative distribution function of a random variable $x$ for value $t$ and parameter values $p_1, \dots, p_k$ .

$P_d(x_{\min}, c_{12}, c_{13})$	Detection probability with threshold $x_{\min}$ and contrasts $c_{12}$ and $c_{13}$ .
$P_\phi(x_{\min}, c)$	False-alarm probability with threshold $x_{\min}$ and edge contrast $c$ .
$\sigma(x, y)$	Associative symmetrical sum of $x$ and $y$ .
$S_d$	Set of detected segments.
$S'_d$	Set of possible connections.
$S = S_d \cup S'_d$	Set of segments.
$G$	Graph of segments.
$\mathcal{L}_i$	Length of a segment $i$ .
$\mathcal{R}_{ij}$	Angle mod $\pi$ between segments $i$ and $j$ .
$c \in C$	Clique $c$ in the set of cliques $C$ .
$p(X = x)$	Probability distribution of the random variable $X$ .
$p(X = x Y = y)$	Conditional probability distribution of $X$ given $Y = y$ .
$L$	Label field.
$D$	Observation field.

## I. INTRODUCTION

THE RECENT launch of numerous radar sensors (ERS-1 and -2, JERS-1, and RADARSAT) as well as their widespread coverage increases the need for automatic or semiautomatic interpretation tools for radar images. In particular, line detection can be used for several applications, such as registration with other sensor images, cartographic applications, and geomorphologic studies. In this paper, we are interested in the detection of the road network on satellite radar images, but the proposed method could be adapted to other images and purposes. In addition, we propose an almost fully automatic method with no need for preselected points (although some parameters have to be set).

Since synthetic aperture radar (SAR) images result from the backscattering of a coherent electromagnetic wave, they present a noisy appearance caused by the speckle phenomenon [1], [2]. Although most of the main axes in the road network may be detected by a skilled human observer looking for dark or bright linear structures, automatic detection remains a difficult task.

In the past 20 years, many approaches have been developed to deal with the detection of linear features on optic [3]–[5] or radar images [6]–[8]. Most of them combine two criteria: a local criterion evaluating the radiometry on some small neighborhood surrounding a target pixel to discriminate lines from background and a global criterion introducing some large-scale knowledge about the structures to be detected.

Manuscript received May 29, 1996; revised December 16, 1996. The work of E. Pechersky was supported by the Russian Foundation of Researches, Grant 96-01-00150.

F. Tupin, H. Maître, and J. M. Nicolas are with École Nationale Supérieure des Télécommunications, 75013 Paris, France (e-mail: maitre@ima.enst.fr).

J. F. Mangin is with the Service Hospitalier Frédéric Joliot, CEA, 91401 Orsay, France.

E. Pechersky is with the Institute for Problems of Information Transmissions, 101 447 Moscow, Russia.

Publisher Item Identifier S 0196-2892(98)00540-3.

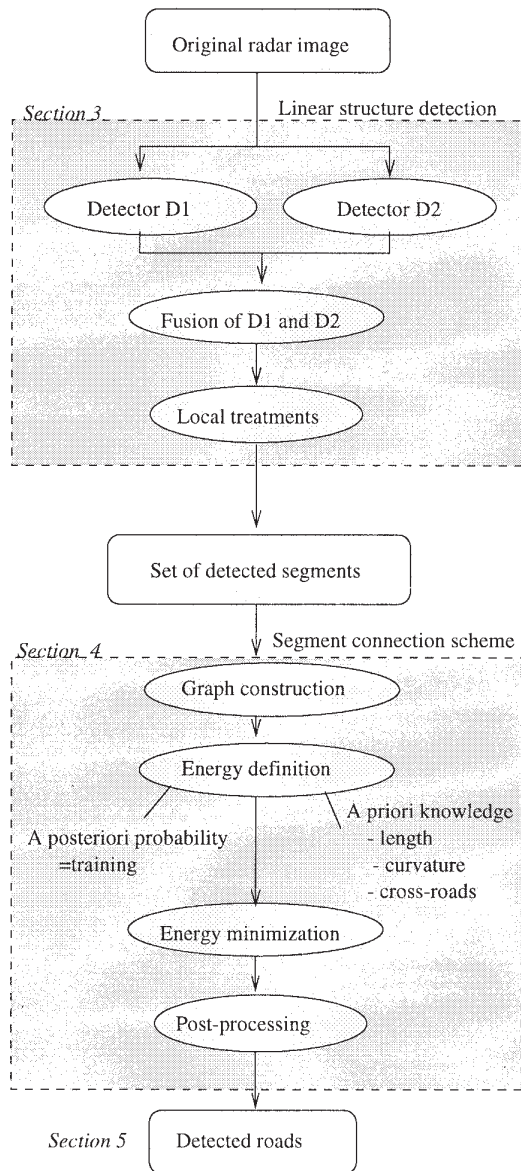


Fig. 1. Diagram showing the different steps and corresponding sections of the proposed method.

Concerning the local criteria, most of the techniques used for road detection in visible range images are based either on conventional edge or line detectors [9]–[11]. They fail in processing SAR images because they often rely on the assumption that the noise is white additive and Gaussian; this is never verified in radar imagery, in which the noise is multiplicative. These methods, therefore, roughly speaking, evaluate differences of averages, implying noisy results and variable false-alarm rates [12], [13]. In the case of radar imagery, local edge or line detectors are often based on statistical properties [14] or on the intensity ratio of neighboring regions [12], [13].

In addition, local criteria are in many cases insufficient for edge or line detection (this is certainly true for radar images), and global constraints must be introduced. For instance, dynamic programming is used to minimize some global

cost functions, as in the original algorithm of Fishler [10] and its improvements [4]. It has also been applied on SAR images in [7] and [15]. Hough-transform-based approaches have also been tested for the detection of parametric curves, such as straight lines or circles [15]–[17]. Tracking methods are another possibility. They find the minimum cost path in a graph by using some heuristics, for instance, an entropy criterion [5]. Energy minimizing curves, such as snakes, have also been applied [18]. The Bayesian framework, which is well adapted for taking some contextual knowledge into account, has been widely used. Regazzoni defines a cooperative process between three levels of a Bayesian network, allowing the introduction of local contextual knowledge as well as more global information concerning straight lines [19]. Hellwich [8] uses *a priori* information concerning line continuity expressed as neighborhood relations between pixels.

The approach proposed in this paper falls within the scope of the Bayesian framework, but a new formulation using segment-sites is developed. Since our aim is to detect the major roads present in an image, contextual knowledge on the scale of pixels (as in [7] and [8]) is insufficient and results in numerous, small, disconnected road segments. However, on the scale of segments a few pixels long, *a priori* knowledge allow for the detection of the main axes in the road network. Thus, we proceed in two steps. In the first step, road-segment candidates are detected. In the second step, a graph of segments is built and a novel Markov random field (MRF) is defined to perform road detection, thus providing a new approach. In the following section, we outline the overall method and the organization of the paper (see also the diagram of Fig. 1).

## II. OVERVIEW OF THE METHOD

The first part of the algorithm performs a local detection of linear structures. It is based on the fusion of the results from two line detectors D1 and D2, both taking the statistical properties of speckle into account. Both detectors have a constant false-alarm rate (that is, the rate of false alarms is independent of the average radiometry of the considered region, as defined in [12]). Line detector D1 is based on the ratio edge detector [12], widely used in coherent imagery, as stated before. This is not a new detector [20], but an in-depth statistical study of its behavior is given. Detector D2, which has emerged from our work, uses the normalized centered correlation between two populations of pixels. Both responses from D1 and D2 are merged to obtain a unique response as well as an associated direction in each pixel. The detection results are postprocessed to provide candidate segments. This first step is described in Section III.

In the second step, our aim is to connect road segments that correspond to true roads. It includes global criteria to cope with the relatively poor detection results from the first step (few segments with large gaps on the real structures and many false detections). Our method relies on a new MRF-based model for roads; this MRF is defined on a set of segments. *A priori* knowledge about the shape of a road is introduced by associating certain potentials to subsets of segments. A simulated annealing algorithm is used to perform the minimization of the

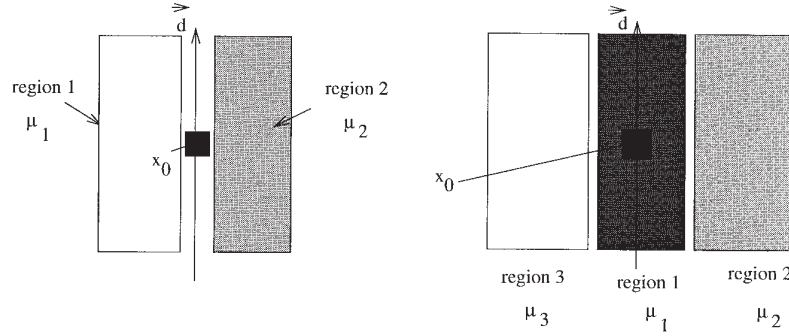


Fig. 2. Vertical edge (on the left) and line (on the right) models used by the detectors.  $\mu_i$  is the empirical mean of region  $i$  computed on  $n_i$  pixels.

MRF associated energy. Some postprocessing is eventually applied to improve detection precision. This second step is described in Section IV.

In Section V, we analyze the influence of parameter setting and, lastly, we provide results on real radar images.

### III. LINE DETECTION

In this section, we discuss detectors D1 and D2 as well as the fusion of their results. Since under certain assumptions, the speckle may be statistically well modeled [21], [22], they are studied through detection and false-alarm probabilities by using either analytical expressions or simulations.

#### A. Ratio Line Detector D1

Letting  $a \exp(i\phi)$  be the complex field received by the sensor, we define the intensity  $I = |a|^2$  and the amplitude  $A = \sqrt{I}$ . This amplitude may have been averaged previously ( $L$ -looks images) by dividing the available bandwidth of the SAR system in  $L$  parts or by spatially averaging  $L$  pixels [23]. The amplitude of pixel  $s$  is noted  $A_s$ , so that the radiometric empirical mean  $\mu_i$  of a given region  $i$  having  $n_i$  pixels is  $\mu_i = (1/n_i) \sum_{s \in i} A_s$ .

The ratio edge detector was introduced in [24] and statistically studied in [12]. Our line detector D1 is derived from the coupling of two such edge detectors on both sides of a region. Let index 1 denote the central region and index 2 and 3 both lateral regions (Fig. 2). We then define the response of the edge detector between regions  $i$  and  $j$  as  $r_{ij}$

$$r_{ij} = 1 - \min\left(\frac{\mu_i}{\mu_j}, \frac{\mu_j}{\mu_i}\right)$$

and the response to D1 as  $r = \min(r_{12}, r_{13})$ , the minimum response of a ratio edge detector on both sides of the linear structure.

With detector D1, a pixel is considered as belonging to a line when its response  $r$  is large enough, i.e., higher than some *a priori* chosen threshold  $r_{\min}$ .

To study the behavior of this detector, its false-alarm and detection probabilities are estimated under the assumption of fully developed speckle, which supposes a rough surface on the wavelength scale [1]. Linear structures and border areas will be considered as rough in a first approximation and a detection occurs when the line detector response is large enough. The

geometric shape of the filter (Fig. 2) is adequate, but many directions have to be tested. Besides, the width of a road not being precisely defined, several widths for region 1 are tried (width from 1 to 3 pixels, corresponding to 12.5–40-m ground widths for ERS-1 PRI images). Thus, considering  $\mathcal{N}_d$  directions  $\mathbf{d}_k$ ,  $k \in \{1, \dots, \mathcal{N}_d\}$  for the line detector,  $3\mathcal{N}_d$  responses are computed (in practice  $\mathcal{N}_d = 8$ ).

Let  $f_x(t|p_1, \dots, p_k)$  be the parametric probability-density function (pdf) of a random variable  $x$  for value  $t$  and parameter values  $p_1, \dots, p_k$ . We denote its cumulative distribution function by  $\Phi_x(t|p_1, \dots, p_k)$ .

Under the hypothesis of the fully developed speckle and with  $\Gamma$  as the Gamma function [25], we obtain an amplitude pdf  $f_A$  for a region of mean-reflected intensity  $\langle I \rangle$  and  $L$ -looks

$$f_A(t|\langle I \rangle) = \frac{2}{\Gamma(L)} \left(\frac{L}{\langle I \rangle}\right)^L t^{2L-1} e^{-(Lt^2/\langle I \rangle)} \quad (1)$$

as described in [1] and [26].

Considering  $r_{ij}$  and  $r$  to be random variables and with  $c_{ij}$  as the exact radiometric contrast between regions  $i$  and  $j$  ( $c_{ij} = \sqrt{\langle I_i \rangle / \langle I_j \rangle}$ ), the pdf of the ratio line detector  $f_r$  is given by (see Appendix I)

$$f_r(t|c_{12}, c_{13}) = \frac{4\Gamma[(n_1 + n_2)L]\Gamma[(n_1 + n_3)L]}{\Gamma(n_1L)^2\Gamma(n_2L)\Gamma(n_3L)} \times n_1^{2n_1L} n_2^{n_2L} n_3^{n_3L} \times \left[ g(t|c_{12}) \int_t^1 g(x|c_{13}) dx + g(t|c_{13}) \int_t^1 g(x|c_{12}) dx \right] \quad (2)$$

where

$$g(x|c_{1i}) = \frac{c_{1i}^{2n_iL} (1-x)^{2n_iL-1}}{[(1-x)^{2n_i} + n_i c_{1i}^2]^{L(n_i+n_i)}} + \frac{\left(\frac{1}{c_{1i}^2}\right)^{n_iL} (1-x)^{2n_iL-1}}{\left[(1-x)^{2n_i} + \frac{n_i}{c_{1i}^2}\right]^{L(n_i+n_i)}}. \quad (3)$$

For given contrasts  $c_{12}$  and  $c_{13}$  between the central region and adjacent regions, the detector has a constant false-alarm rate, independent of the gray levels. We call this a constant false-alarm detector. Examples of such functions  $f_r(t|c_{12}, c_{13})$  are presented in Fig. 3.

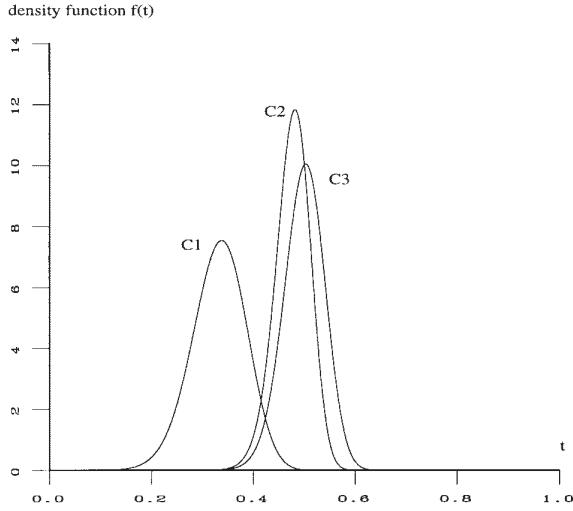


Fig. 3. Density function  $f_r(t)$  for the line detector D1 and for different contrasts, with  $n_1 = 33$ ,  $n_2 = n_3 = 22$ .  $C_1$ :  $c_{12} = 2$ ,  $c_{13} = 1.5$ ;  $C_2$ :  $c_{12} = c_{13} = 2$ ; and  $C_3$ :  $c_{12} = 2$ ,  $c_{13} = 4$ .

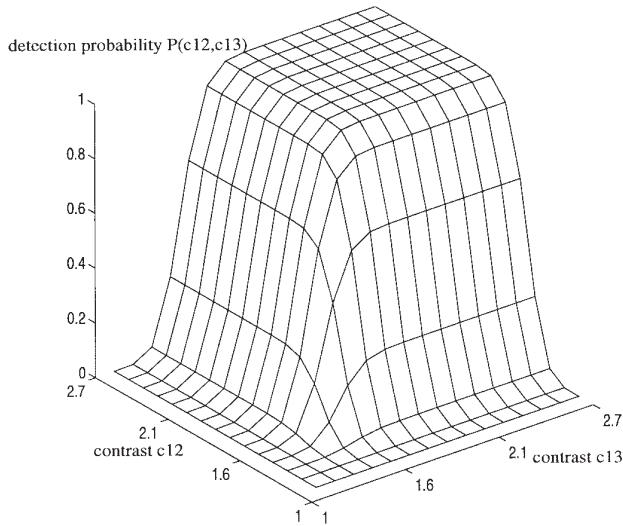


Fig. 4. Probability of detection versus the contrasts  $c_{12}$  and  $c_{13}$  with the decision threshold  $r_{\min} = 0.3$  and  $n_1 = 33$ ,  $n_2 = n_3 = 22$  for the line detector D1.

The detection probability  $P_d$ , corresponding to a decision threshold  $r_{\min}$  and the contrasts  $c_{12}$  and  $c_{13}$ , is (Fig. 4)

$$P_d(r_{\min}, c_{12}, c_{13}) = \int_{r_{\min}}^1 f_r(t|c_{12}, c_{13}) dt.$$

For a given direction, false detections occur in two cases: on homogeneous windows ( $c_{12} = c_{13} = 1$ ) and on edges ( $c_{12} = 1$  or  $c_{13} = 1$ ). In both cases and for a given decision threshold  $r_{\min}$ , the false-alarm probability  $P_\phi$  is given by

$$\begin{aligned} P_\phi(r_{\min}, c) &= P_d(r_{\min}, 1, c) = P_d(r_{\min}, c, 1) \\ &= \int_{r_{\min}}^1 f_r(t|1, c) dt. \end{aligned} \quad (4)$$

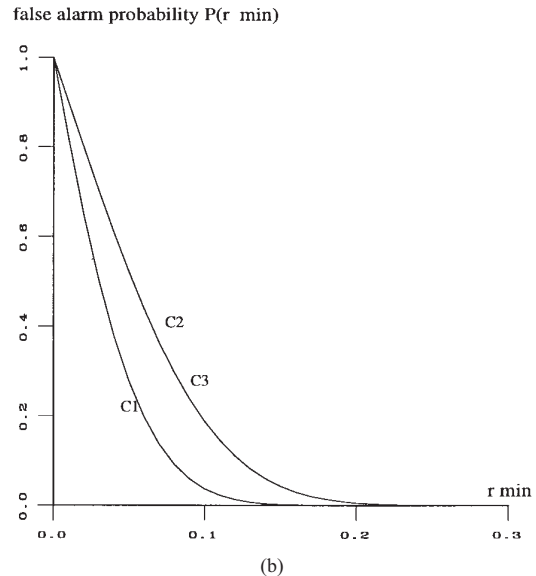
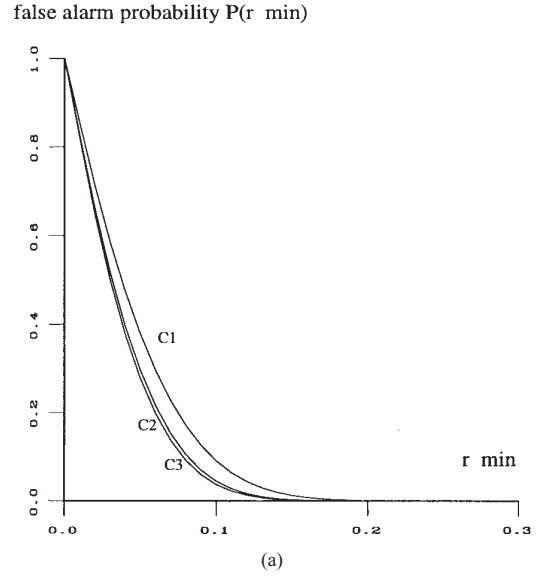


Fig. 5. False-alarm probabilities  $P_\phi(r_{\min}, c)$  versus  $r_{\min}$  and analysis of the influence of different parameters for the line detector D1. (a) Pixel number influence on a homogeneous area;  $C_1$ :  $n_1 = 11$ ,  $n_2 = n_3 = 33$ ;  $C_2$ :  $n_1 = n_2 = 22$ ,  $n_3 = 33$ ; and  $C_3$ :  $n_1 = 33$ ,  $n_2 = n_3 = 22$ . (b) Edge contrast  $c$  influence;  $C_1$ :  $c = 1$ ;  $C_2$ :  $c = 2$ ; and  $C_3$ :  $c = 4$ .

Thus, the decision threshold  $r_{\min}$  can be deduced from the statistical behavior of the detector. As usual, the detection probability increases with a decreasing decision threshold, but at the same time, the false-alarm rate increases [Fig. 5(a) and (b)]. Therefore,  $r_{\min}$  may be deduced as a compromise between a chosen false-alarm rate and a minimum detectable contrast.

To test the correspondence between theoretical and practical results, a homogeneous area has been selected in an ERS-1 image. It corresponds to a region with fully developed speckle, whose measured pdf is close to that given in (1) [Fig. 6(a) and (b)]. Let  $\mathcal{H}_0$  denote the hypothesis that the sample follows the theoretical distribution (1); let  $\mathcal{H}_1$  denote the hypothesis that

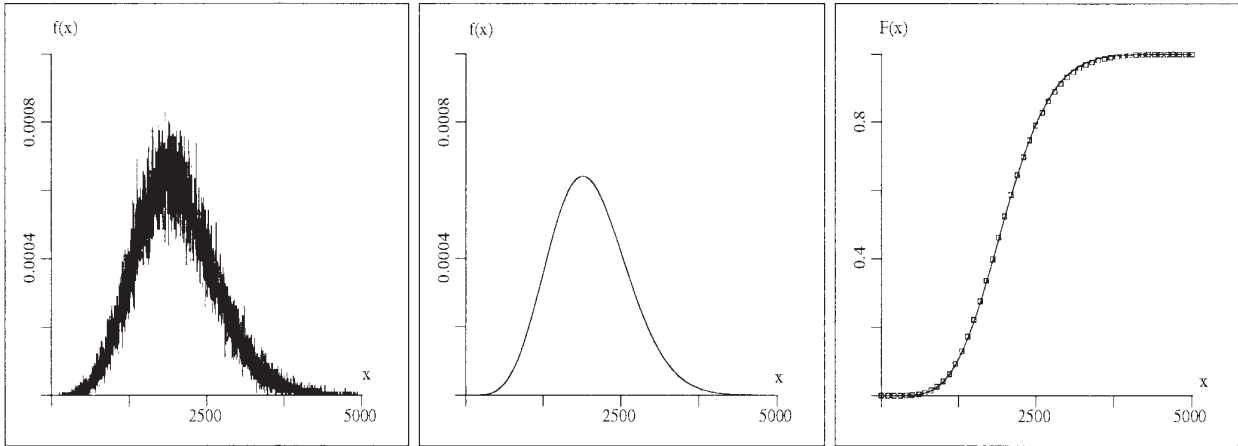


Fig. 6. Statistical study of the homogeneous test area. (a) Histogram of the amplitudes measured on the homogeneous test area. (b) Theoretical probability-density function corresponding to (1). (c) Probability  $F(x)$  for the amplitude to be less than the value  $x$ : the theoretical probability with an unbroken line, and the measured one on the test area indicated by a series of points. Their difference is used to obtain the Kolmogorov-Smirnov test response.

TABLE I  
NUMBER OF PIXELS FOR CENTRAL AND ADJACENT REGIONS,  
FOR DIFFERENT WIDTHS OF THE CENTRAL REGION

Width of the central line	Number of pixels of region 1	Number of pixels of region 2	Number of pixels of region 3
1	11	33	33
2	22	22	33
3	33	22	22

it does not; and let  $\alpha$  denote the probability of choosing  $\mathcal{H}_1$  when  $\mathcal{H}_0$  is true (first-kind risk). A Kolmogorov-Smirnov test applied with  $\alpha = 0.01$  is positive, meaning that the behavior of the sample corresponds to the theoretical prediction with a first-kind risk of 1% [27] [Fig. 6(c)]. On this test area, which does not contain any road (as it was selected from a sea area), the false-alarm rates that are a function of the threshold  $r_{\min}$  are measured and compared to theoretical false-alarm rates. To take into account the correlation between pixels (interpixel spacing of 12.5–25-m resolution cell), an equivalent number of looks is used for each  $n_i$  value. Fig. 7(a) shows a good agreement between theoretical and practical results in the case of a sea ERS-1 area, confirming our hypotheses.

The size of the detection mask is chosen to contain enough pixels in each region and to respect the shape of the road. Indeed, the more pixels we use to compute the empirical means, the less number of false alarms [Fig. 5(a)]. We use a length of 11 pixels and a total width of 7 pixels (mask  $11 \times 7$  pixels). The number of pixels for central and adjacent regions, for different widths of the central region are given in Table I.

Besides, as already mentioned, the line detector responses have to be computed in many directions. Because of the chosen length of the mask, at least eight directions have to be used to guarantee that any road, whatever its direction, has the same detection probability. Therefore, at each pixel, 24 different measures are obtained. Mask sizes are chosen as a compromise. On the one hand, the neighborhood must be as large as possible to reduce false-alarm rates; on the other

hand, the direction number must be small enough to limit computation time.

When line detection using only D1 is performed, after having measured the response of the filter in  $\mathcal{N}_d$  directions, we keep the best response. This multidirection detector has a different false-alarm rate than the one given by (2). Let  $P_{\phi_{\mathcal{N}_d}}$  denote the false-alarm probability for  $\mathcal{N}_d$  directions. Touzi *et al.* [12] have suggested the following empirical expression for the edge detector:

$$P_{\phi_{\mathcal{N}_d}} = 1 - (1 - P_{\phi_1})^\alpha$$

with  $\alpha = 3$ , when  $\mathcal{N}_d = 4$ . For the line detector, we found experimentally that a similar expression is adequate, with  $\alpha = 5$  in the case of  $\mathcal{N}_d = 8$  [Fig. 7(b)]. The decision thresholds used in practice can be deduced from these results.

### B. Cross-Correlation Line Detector D2

In this section, we present a second detector for lines called D2, based on a new edge detector that we present first.

Our approach is inspired from the work of Hueckel [28]. The ideal step-edge best approximating the amplitude in a given window  $V_{x_0}$  around a pixel  $x_0$  and for a given direction  $\mathbf{d}_k$  ( $k \in \{0, \dots, \mathcal{N}_d\}$ ) is computed by using the mean square error minimum criterion. This edge is, in this case, composed of two regions  $i$  and  $j$  with constant values  $\mu_i$  and  $\mu_j$ . Once this ideal edge is defined, the validity of the hypothesis “there is an edge in  $x_0$  with the direction  $\mathbf{d}_k$ ” is tested by using the normalized-centered cross-correlation between pixels of  $V_{x_0}$  and the ideal edge. The cross-correlation coefficient  $\rho_{ij}$  can be shown to be (see Appendix II)

$$\rho_{ij}^2 = \frac{1}{1 + (n_i + n_j) \frac{n_i \gamma_i^2 \bar{c}_{ij}^2 + n_j \gamma_j^2}{n_i n_j (\bar{c}_{ij} - 1)^2}}$$

where  $n_i$  is the pixel number in region  $i$ ,  $\bar{c}_{ij} = \mu_i/\mu_j$  is the empirical contrast between regions  $i$  and  $j$ , and  $\gamma_i$  is the variation coefficient (ratio of standard deviation and mean) that

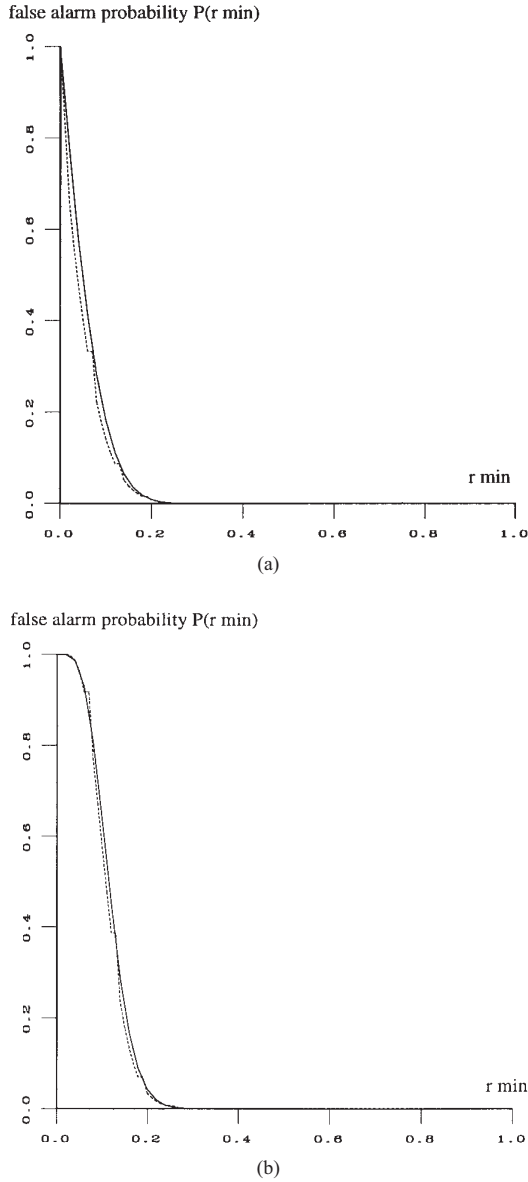


Fig. 7. Comparison of the theoretical (in full line) false-alarm probability  $P_{\phi}(r_{\min}, 1)$  versus  $r_{\min}$  and the frequencies obtained on an ERS-1 homogeneous test area for the line detector D1 in dotted line. (a) In the case of the response in one direction. (b) In the case of the response in eight directions (the best response is kept).

adequately measures homogeneity in radar imagery scenes. This expression depends on the contrast between regions  $i$  and  $j$ , but also takes into account the homogeneity of each region, thus being more coherent than the ratio detector (which may be influenced by isolated values). In the case of a homogeneous window,  $\mu_i = \mu_j$ ,  $\rho_{ij}$  equals zero, as expected.

As in the previous section, the line detector D2 is defined by the minimum response  $\rho$  of the filter on both sides of the structure  $\rho = \min(\rho_{12}, \rho_{23})$ . A line is detected when the response is higher than the decision threshold  $\rho_{\min}$ . For the statistical study, the pdf of  $\rho$  must be estimated. Because of the dependency between the mean and the standard deviation of

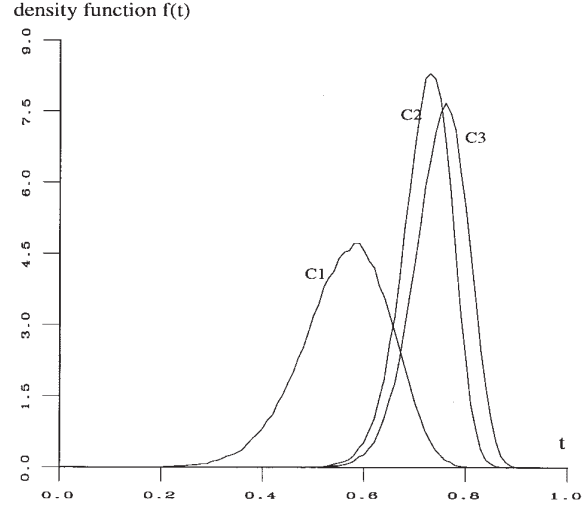


Fig. 8. Density function  $f_{\rho}(t)$  for the line detector D2 and different contrasts with  $n_1 = 33, n_2 = n_3 = 22$ :  $C_1: c_{12} = 2, c_{13} = 1.5$ ;  $C_2: c_{12} = c_{13} = 2$ ; and  $C_3: c_{12} = 2, c_{13} = 4$ .

region  $i$ , an explicit expression is difficult to derive. To study the behavior of the detector, simulations are used.

For each region of given mean intensity  $\langle I_i \rangle$ ,  $n_i$  amplitude values are selected by using the pdf described by (1) and random realizations are computed. This process is iterated (100 000 times) and the occurrences of  $\rho$  are used to approximate its pdf (Fig. 8).

As for the ratio line detector D1, responses are computed in eight directions on a  $7 \times 11$ -pixel mask, and for three different widths of the central line (widths ranging from 1 to 3 pixel are tested).

In the case of homogeneous regions, the results of both line detectors are very similar, as can be seen by comparing Figs. 4 and 9 as well as Figs. 5 and 10. We also find a good agreement between theoretical and practical results by using the same homogeneous test area, in the case of one and eight directions.

### C. Fusing Responses from D1 and D2

In practice, the ratio line detector D1 is less accurate (multiple responses to a structure), but also less sensitive to the hypotheses, taking into account only the contrast between the regions (Fig. 11). Therefore, we decided not to choose one of them, but to merge information from both D1 and D2 in each direction by using an associative symmetrical sum  $\sigma(x, y)$ , as defined in [29]

$$\sigma(x, y) = \frac{xy}{1 - x - y + 2xy}, \quad \text{with } x, y \in [0, 1]. \quad (5)$$

This fusion operator has been chosen because of its indulgent disjunctive behavior for high values ( $x > 0.5, y > 0.5$ ), its severe conjunctive behavior for small values ( $x < 0.5, y < 0.5$ ), and its adaptative behavior, depending on  $x$  and  $y$  values in the other cases.

Since the behavior of this operator depends on the position of the responses compared to the value 0.5, we first centered both D1 and D2 responses before applying the fusion, so that

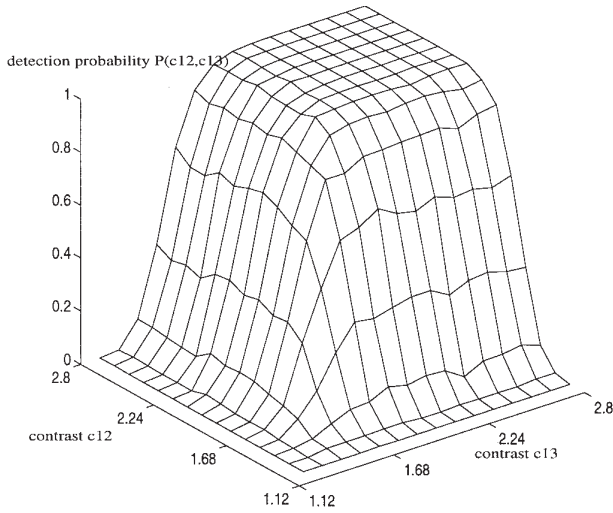


Fig. 9. Detection probability versus the contrasts  $c_{12}$  and  $c_{13}$  with the decision threshold  $\rho_{\min} = 0.6$  and the pixel numbers  $n_1 = 33$ ,  $n_2 = n_3 = 22$  for the line detector D2.

the decision thresholds correspond to 0.5. In order to do so and constraining both  $r$  and  $\rho$  to lie in the interval  $[0, 1]$ , we replace them by  $\max[0, \min(1, x+0.5-x_{\min})]$ , where  $x$  equals  $r$  and  $\rho$ , respectively. As a result, the decision threshold applied on  $\sigma(r, \rho)$  is automatically the central value 0.5 of interval  $[0, 1]$ .

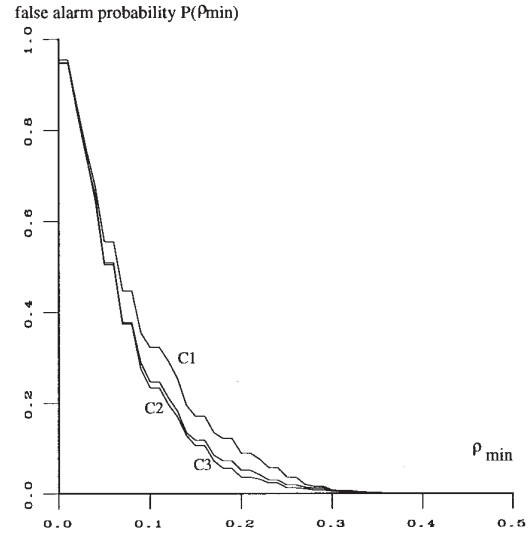
Once again, for the statistical study, simulations have been used since no analytical expression of the pdf for  $\sigma(r, \rho)$  is available (random variables  $r$  and  $\rho$  are of course not independent). For the response after fusion, the false-alarm rate is a function of  $r_{\min}$  and  $\rho_{\min}$ ; an example is shown in the case of a homogeneous area [Fig. 12(a)]. Fig. 12(b) shows the detection probability using  $r_{\min}$  and  $\rho_{\min}$ , which guarantees a false-alarm rate less than 1%. Using the same test area as before, a good agreement between practical and theoretical results has been found, as was also the case for D1 and D2, separately.

Eventually, in order to obtain a unique response in each pixel, the best response in any of the  $\mathcal{N}_d$ -tested directions is kept along with the associated direction  $\mathbf{d}_k$ ,  $k \in \{0, \dots, \mathcal{N}_d\}$ . The response image is thresholded with a threshold of 0.5, resulting in a binary image and an image of the directions.

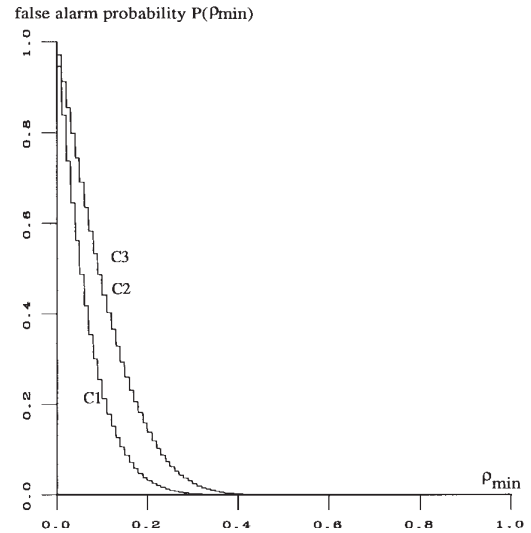
#### D. From Pixels to Segments

Starting from the response of the line detector at each pixel, we now generate segment primitives for further processing by the following procedures, whose aim is to suppress local false alarms and obtain a "cleaner" binary result by using simple heuristic rules.

- Since isolated pixels have little chance of belonging to a road, a pixel suppression step is first performed. For each pixel kept with direction  $\mathbf{d}_k$ ,  $k \in \{0, \dots, \mathcal{N}_d\}$ , we look for other selected pixels with a direction close to  $\mathbf{d}_k$  (i.e.,  $\mathbf{d}_{k+1}$ ,  $\mathbf{d}_k$ , or  $\mathbf{d}_{k-1}$ ) in an angular beam around it. If none is found, the pixel is suppressed.
- In order to suppress other dubious responses due to small local structures, the best line in a given neighborhood



(a)



(b)

Fig. 10. False-alarm probabilities  $P_\phi(\rho_{\min}, c)$  versus  $\rho_{\min}$  and analysis of the influence of different parameters for the line detector D2. (a) Pixel number influence on a homogeneous area;  $C_1$ :  $n_1 = 11$ ,  $n_2 = n_3 = 33$ ;  $C_2$ :  $n_1 = n_2 = 22$ ,  $n_3 = 33$ ; and  $C_3$ :  $n_1 = 33$ ,  $n_2 = n_3 = 22$ . (b) Edge contrast  $c$  influence;  $C_1$ :  $c = 1$ ;  $C_2$ :  $c = 2$ ; and  $C_3$ :  $c = 4$ .

is detected. To do so, a local Hough transform [30] is applied on a  $20 \times 20$ -pixel tiling of the image with a half-window overlap. Each pixel is attributed a vote for its associated direction. The straight line having the highest count is selected. Only the pixels with votes for the accepted line are kept, the others are suppressed.

- The next step aims to fill small gaps between selected pixels. Pixels are linked in the direction  $\mathbf{d}_k$  of any pixel; the pixels belonging to an angular beam around  $\mathbf{d}_k$  with a direction close to  $\mathbf{d}_k$  and at a distance less than four pixels are linked to it.
- Segments are finally obtained by thinning the binary image [31], and a polygonal approximation step gives a vectorial representation of the segments.

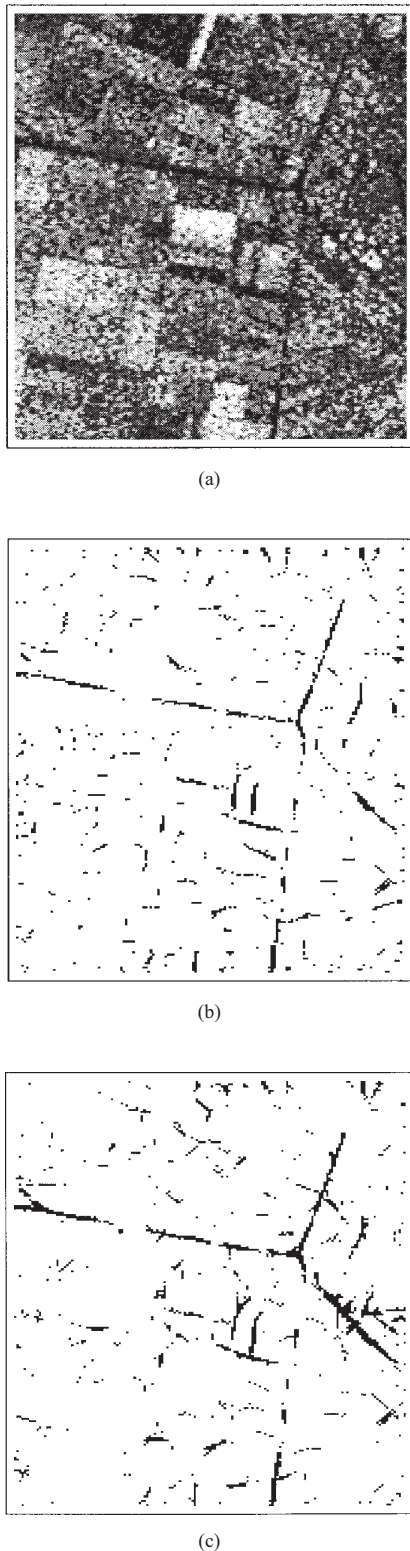


Fig. 11. Comparison of the detector responses on an ERS-1 SAR image. Both thresholds are chosen to insure false-alarm rates less than 1%. Detector D1 gives less-accurate responses than D2, but is less sensitive to the hypothesis of homogeneous areas, as seen in the right part of the image where specular bright points are along the road. (a) Part of an ERS-1 image of The Netherlands. (b) Thresholded responses of the line detector D2. (c) Thresholded responses of the line detector D1.

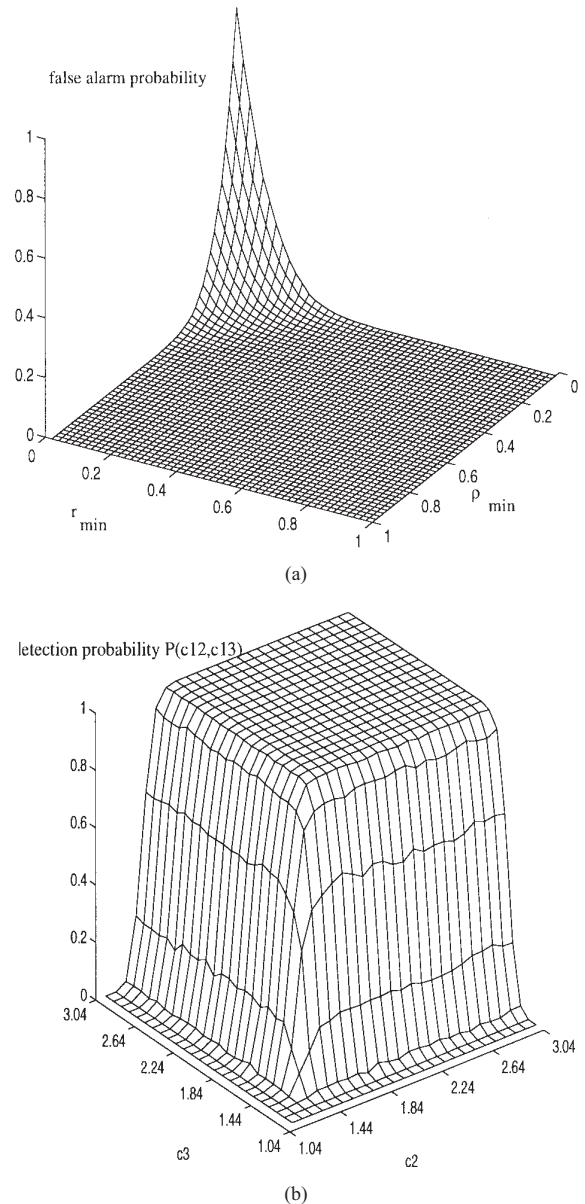


Fig. 12. Behavior of the fusion  $\sigma(r, \rho)$  of both D1 and D2 recentered responses  $r$  and  $\rho$ . (a) False-alarm probability versus  $r_{\min}$  and  $\rho_{\min}$  on an homogeneous area. (b) Detection probability versus the contrasts  $c_{12}$  and  $c_{13}$ . Both thresholds  $r_{\min}$  and  $\rho_{\min}$  are chosen to insure false-alarm rates less than 1% ( $r_{\min} = 0.25$  and  $\rho_{\min} = 0.45$ ).

#### IV. NETWORK GLOBAL INTERPRETATION BASED ON A MARKOVIAN FIELD DEFINED ON A SET OF SEGMENTS

##### A. Introduction

As already mentioned in the Introduction, a necessary step for all edge detection methods using local detectors is the closing stage; starting from local information (for instance, a gradient map), a more global one must be deduced (the extracted edges) by a grouping process. An abundance of literature covers this subject, reporting on many different approaches [32]–[35]. But most of these works deal with high-quality images and perform segment linking at the scene-

analysis level. Unfortunately, SAR images do not allow for such methods because of the poor performance of the low-level detection stage.

In the following, we introduce the Markovian framework as a tool for grouping in the case of poor local detection, since contextual *a priori* knowledge is generally sufficient to identify roads. A graph is built from the detected segments and the road identification process is modeled as the extraction of the best graph labeling.

An indexation of the random process by segment is a natural choice for road detection purposes. A similar approach has been proposed by Marroquin [36], who defined a MRF of piecewise straight lines associated with pixel sites. It is not the case here, as our primitives are the vectors detected in the previous stage, as in [37]. This choice results in a nonuniform topology of the graph.

### B. Graph Definition

Let us denote by  $S_d$  the set of detected segments at the end of the previous stage (Section III-D). Among these segments, some belong to the real roads, others are false detections. Many parts of the roads also remain undetected. We make the assumption that the true road network may be obtained by connecting these detected segments in an appropriate way and by rejecting the false detections. Thus, we add the set  $S'_d$  of all possible connections to  $S_d$ . A connection is possible if it verifies the following three conditions:

- it links two endpoints of two different segments;
- endpoints are close enough (i.e., the distance between them is less than a fixed threshold  $\mathcal{D}_{\max}$ );
- alignment of the two segments is acceptable.

Let the segment  $i$  belong to  $S_d$ , and let  $M_i^k$  with  $k \in \{1, 2\}$  denote  $i$  endpoints ( $i = M_i^1 M_i^2$ ). Denoting the “possible-connection” relationship between two segments  $i$  and  $j$  of  $S_d$  by  $iAj$ , we define

$$S'_d = \{M_i^k M_j^l, i \in S_d, j \in S_d \text{ and } iAj\}.$$

Hence, we built a new set  $S$  of segments as the union of  $S_d$  and  $S'_d$ :  $S = S_d \cup S'_d$ .  $S$  is endowed with a graph structure, each segment  $i$  (real or possible) being a node, and two nodes  $i$  and  $j$  being linked by an arc if they share a common endpoint. In order to define a MRF on this graph denoted by  $G$ , we define the neighborhood  $\mathcal{V}_i$  of node  $i$  as the set of nodes adjacent to it

$$\mathcal{V}_i = \{j \in S / \exists (k, p) \in \{1, 2\}^2, M_i^k = M_j^p, j \neq i\}.$$

The cliques of the graph  $G$  are all subsets of segments sharing an extremity, including singletons and cycles of three segments. Attributes are attached to the nodes and the arcs of  $G$  to construct an attributed relational graph  $G_a$ , taking into account geometric properties. To each graph node,  $i$  is associated the segment length divided by  $\mathcal{D}_{\max}^1$  and denoted by  $\mathcal{L}_i$  (therefore  $\mathcal{L}_i \in [0, 1]$ ), and to each arc between nodes  $i$  and  $j$ , the angle  $\mathcal{R}_{ij} \bmod \pi$  between the two segments.

Road detection consists in identifying nodes belonging to a road, i.e., in labeling the graph. A binary variable  $L_i$  is therefore associated with node  $i$ ;  $L_i = 1$  if  $i$  belongs to a road

<sup>1</sup> $\mathcal{D}_{\max}$  will serve in the following as a scale factor that may be adjusted independently on every scene.

and  $L_i = 0$  if not.<sup>2</sup> With  $N$  as the cardinal of  $S$ , the label random field  $L = (L_1, L_2, \dots, L_N)$  takes its values in  $\Omega$ , the set of all possible configurations with cardinality  $2^N$ . In all of the following,  $p$  denotes a probability distribution, which might depend on graph attributes.

The result of the road detection is defined as the most probable configuration for  $L$  given the observation process  $D$  for the segments of  $S$ , with a MAP criterion. It means that the solution corresponds to the maximum of the conditional probability distribution of  $L$  given the observation  $D$ :  $p(L|D)$  (also called posterior probability distribution). Using Bayes rule

$$p(L|D) = \frac{p(D|L)p(L)}{p(D)} \quad (6)$$

and instead of the posterior probability distribution,  $p(L)$  and  $p(D|L)$  have to be estimated. The conditional probability distribution of the observation field  $p(D|L)$  stems from a supervised learning step on known areas, and the *a priori* probability distribution  $p(L)$  relies on a Markovian model of usual roads.

### C. Conditional, Prior, and Posterior Probability Distributions

The process  $L$  conditionally to  $D$  (noted  $L|D$ ) is modeled as a Markovian field by using the equivalence between MRF and Gibbs fields.

1) *Conditional Distribution of the Observation Field  $D$ .*  $p(D|L)$ : Let us first define the observation process  $D = (D_1, D_2, \dots, D_N)$  deduced from the line detector of the first step. The two detector responses are first computed for each pixel belonging to a segment  $i$  of  $S$ ; the three regions of the mask being defined along the segment for the central region and on both sides of the segment for the adjacent regions. The two responses are then merged by using (5), and the mean, computed on all the pixels belonging to the segment, gives the observation  $d_i$  associated to  $i$ .

Under the assumption of independence between the  $D_i$  and supposing that  $D_i$  conditional probability distribution only depends on  $L_i$ , we may write

$$p(D|L) = \prod_{i=1}^N p(D_i|L) = \prod_{i=1}^N p(D_i|L_i) \propto \exp \left[ - \sum_{i=1}^N V(d_i|l_i) \right]$$

where  $V(d_i|l_i)$  denotes the potential of segment  $i$ . The conditional probability distributions  $p(D_i|L_i)$  are learned from an experiment after a manual segmentation of roads by a human observer. They are presented in Fig. 13. Using these results, the linear potentials shown in Fig. 14 have been chosen, which verify

$$\begin{aligned} V(D_i = d_i|L_i = 0) &= 0, & \text{if } d_i < t_1 \\ V(D_i = d_i|L_i = 0) &= 0 \frac{d_i - t_1}{t_2 - t_1}, & \text{if } t_1 < d_i < t_2 \\ V(D_i = d_i|L_i = 0) &= 1, & \text{if } d_i > t_2 \\ V(D_i = d_i|L_i = 1) &= 0, & \forall d_i. \end{aligned}$$

<sup>2</sup>In the following, all random fields will be denoted by capital letters and their realizations in small ones.

Since a road segment may have almost any observation value  $d_i$ , all segments are penalized in the same way for label 1. The potential value has been chosen zero, which fulfills the normalization constraint

$$\begin{aligned} & \int_0^1 p(D_i = t | L_i = 1) dt \\ &= \int_0^1 \exp[-V(D_i = t | L_i = 1)] dt = 1. \end{aligned}$$

In the same way, potentials for label 0, although corresponding to the previous observations (Fig. 14), are not normalized. To obtain a correspondence between potentials and probability distributions, potentials of the form  $V(D_i = d_i | L_i = 0) + \log Z$  are used;  $Z$  being the normalization constant, which implies  $Z = t_1 + (1 - t_2)(1/e) - (t_2 - t_1)(1/e - 1)$  with  $e = \exp(1)$ . Since  $Z < 1$ , we have  $\log Z < 0$ .

2) *Prior Distribution of the Label Field  $L$ .  $p(L)$ :* If we assume that the detection of a road can be deduced from local contextual knowledge,  $L$  can be expressed as a MRF, and using the MRF-Gibbs field equivalence (Hammersley-Clifford theorem [38])

$$p(L = l) = \frac{1}{Z'} \exp[-U(l)]$$

where  $Z'$  is a normalizing constant,  $C$  denotes the clique set, and  $U(l) = \sum_{c \in C} V_c(l)$ . Clique potentials are chosen to express the following *a priori* knowledge about roads:

- 1) roads are long (they should almost never stop);
- 2) roads have a low curvature;
- 3) intersections are rare (i.e., a segment is more often connected to a unique other segment in one of its extremities than to many segments, at least in nonurban areas).

As a consequence, a road is modeled as an infinite succession of segments with low curvature. The third condition does not forbid crossroads, but gives them a lower probability than the connection between only two segments. The flexibility of the Gibbs-field framework allows us to construct simple potentials endowing the random field with a probability distribution stemming from these *a priori* knowledge.

All clique potentials  $V_c(l)$  are null except for the cliques of highest order corresponding to the sets of segments sharing the same common extremity for all segments, which turns out to be sufficient for modeling all the interactions between road segments defined above. For a clique  $c$  of this sort, we define

$$\begin{aligned} \forall i \in c, l_i = 0 &\Rightarrow V_c(l) = 0 \\ \exists! i \in c / l_i = 1 &\Rightarrow V_c(l) = K_e - K_{\mathcal{L}} \mathcal{L}_i \\ \exists!(i, j) \in c^2 / l_i = l_j = 1, \mathcal{R}_{ij} > \frac{\pi}{2} &\Rightarrow V_c(l) \\ &= -K_{\mathcal{L}} (\mathcal{L}_i + \mathcal{L}_j) + K_c \sin \mathcal{R}_{ij} \\ \text{in all other cases } V_c(l) &= K_i \sum_{i/i \in c} l_i. \end{aligned}$$

All parameters are connected in a simple way with the three previously expressed road characteristics. Choosing  $K_e > 0$  and  $K_{\mathcal{L}} > 0$  fulfills condition i) and favors long roads

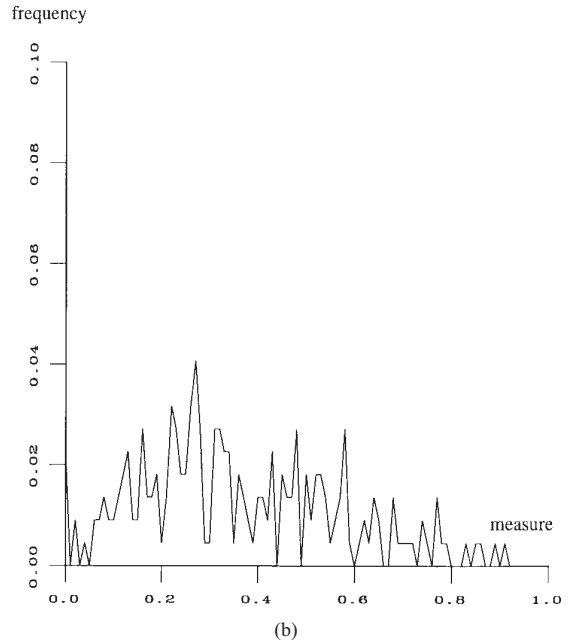
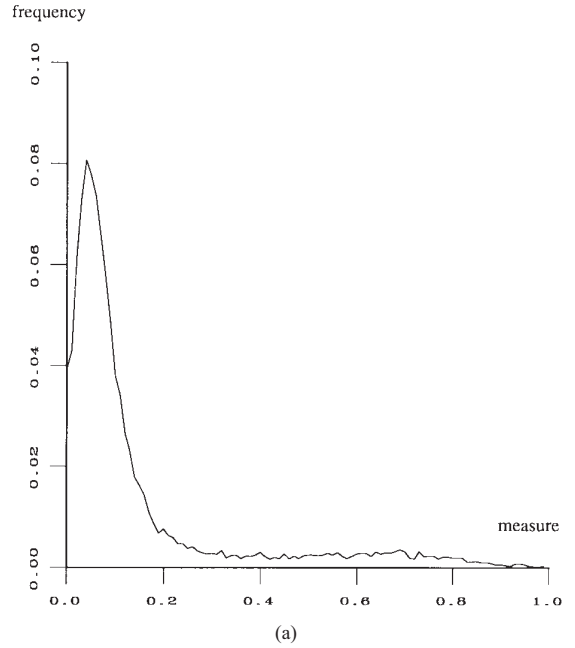


Fig. 13. Conditional frequencies of the observations on a part of an image of The Netherlands. Under stationarity and ergodicity hypotheses, posterior probability potentials are derived from them. (a) Measure frequencies on nonroad segments. Almost all of them have a measure lower than 0.2, making easy discrimination possible. (b) Measure frequencies on structures (roads) manually detected. The density function is almost uniform, and all measures are possible along the road. Indeed, road-local visibility may change drastically depending on the surrounding objects: dark fields, relief, and partial covering by human or natural structures lead to low measures.

(extremity penalization and length reward).  $K_c > 0$  penalizes road configurations with high curvatures fulfilling condition ii), whereas  $K_i > 0$  puts crossroads at a disadvantage, which corresponds to condition iii). Without the observation field, a unique very long road connecting all segments and showing low curvature is obtained.

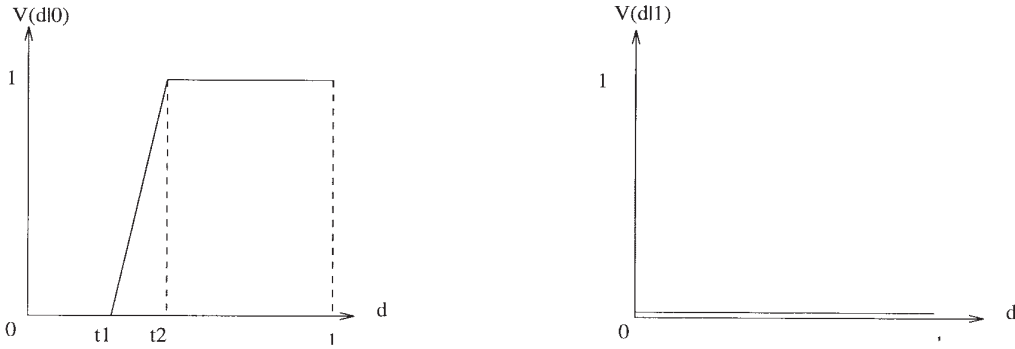


Fig. 14. Non-normalized linear potential  $V(D_i = d|L_i = 0)$  and  $V(D_i = d|L_i = 1)$  versus the observation  $d$  of  $i$  deduced from the observation conditional frequencies.

3) *Posterior Distribution*.  $p(L|D)$ : Since  $p(D|L)$  and  $p(L)$  correspond to Gibbs distributions defined on the same graph, so does the global-field probability distribution. Therefore,  $L|D$  is a MRF defined on  $\Omega$ , with global energy

$$U(l|d) = \sum_{i=1}^N V(d_i|l_i) + \sum_{c \in C} V_c(l).$$

Potentials are those previously defined as  $V(d_i|l_i)$  in the conditional distribution and  $V_c(l)$  in the prior distribution. The first represent the attachment to the data and the second contextual information. In practice, weighted first-order potentials are used, taking into account the length  $\mathcal{L}_i$  of the segment  $[\mathcal{L}_i V(d_i|l_i)$  instead of  $V(d_i|l_i)$ ]. In that way, more importance is given to observations along long segments. For the sake of simplicity, we do not take into account this change in the normalizing constant for posterior potentials.

#### D. Dedicated Simulated Annealing

Since  $p(D|L) = [\exp -U(d|l)]/Z_{norm}$ , the MAP configuration corresponds to the energy minimum. Since the energy function is nonconvex, a stochastic minimization algorithm has been chosen. But because practical implementations of the simulated annealing scheme only approximate the theoretical framework, Geman's fundamental result of convergence [39] is not valid in practice. In spite of a rapid decrease in temperature and a finite number of iterations, results are generally satisfying and globally stable. Nevertheless, in the case of some particular energy landscapes, unwanted behavior is observed and problem-dedicated minimization algorithms are used [40]. This is our case, due to the presence of many local minima. Indeed, results obtained with a fixed parameter set and different initializations may differ a lot. An empirical solution has been used, giving good results. Instead of considering sequentially each node and its label change, sets of adjacent nodes are considered. Hence, the Gibbs Sampler algorithm is applied on sets of sites. A theoretical study should be made to validate this method, which consists of adapting the exploration topology of annealing to the specific energy landscape, but experimentally it has been shown that this approach is well adapted to our problem. In this case, we have considered sets of three adjacent segments, which provide

eight possible configurations of labeling. The Gibbs Sampler is applied on the eight corresponding energy states. This method helps the process to leave local minima by comparing very different configurations like the three segments labeled as one with all three labeled as zero. When only one segment is considered sequentially instead of three connected segments, a very high initial temperature has to be set to provide a stable result. Sets of four or more segments can be considered, but sets of three segments provide satisfying results.

Using deterministic algorithms, like iterated conditional modes (ICM), with a good initialization (for instance, labeling as one all the segments detected by the first step and as zero all the others) always provide local minima—the same exploration topology with sets of three segments is used. Results are close to the global minimum result, but they are not stable, and a slightly different realization is obtained for each minimization.

#### E. Postprocessing

Since roads are obtained as segment chains, they are not precisely located. For road visualization, a simplified snake-based method has been used [32]. The external forces are energy functionals attracting snakes to specified image features. Here, these features are dark (or bright) areas in the image corresponding to the roads. Thus, the radiometric image (or its inverse) is used as external energy. The internal forces correspond to a regularization term imposing some smoothness on the curves. In this simplified version, return spring forces are used, penalizing large deviations from the initial position.

### V. PARAMETER SETTING AND VALIDATION

Before presenting some experimental results on radar images, we first discuss the parameters that are needed and analyze their influence on the final results.

#### A. Parameters of the Line Detection Step

Two parameters must be set in this step: the decision thresholds  $r_{\min}$  and  $\rho_{\min}$  (the decision threshold on the fusion measure is fixed to 0.5). Although the theoretical study does only provide the thresholds in a theoretical case for three perfectly homogeneous regions for the road and the adjacent

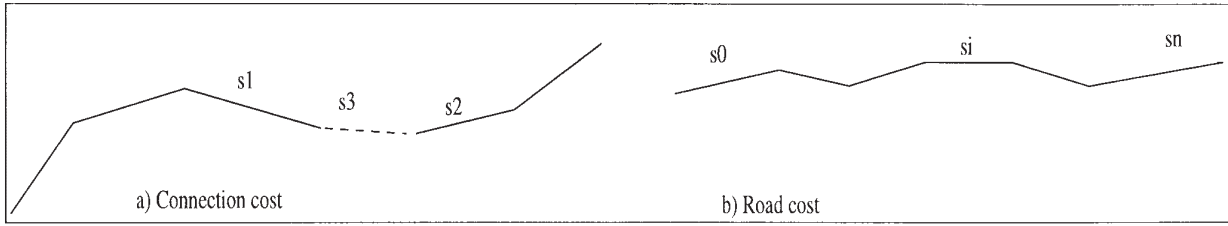


Fig. 15. Analysis of some particular configurations to limit parameter intervals. Energy comparison between an unconnected and a connected configuration (a) and comparison between a road configuration (b) and the configuration with all segments set to label 0.

regions, it gives us a basis for performing an empirical study. Besides, both thresholds have shown to be quite robust for a specific sensor, and the same values have been used on all ERS-1 images we tested.

### B. Parameters of the Global Connection Step

A usual difficulty with MRF's is the choice of the distribution parameters, which balance different kinds of interactions. Here, these constants ( $K_e$ ,  $K_{\mathcal{L}}$ ,  $K_i$ , and  $K_c$ ) are chosen by considering some particular configurations.

Let us first define the “null configuration” as the configuration where all segments have label zero.

First, because two segments should not be systematically connected, the energetic variation  $\Delta U$  between the connected and unconnected configurations should be positive in an unfavorable case [Fig. 15(a)].

$$\Delta U = -2K_{\mathcal{L}}\mathcal{L}_3 + K_c(\sin \mathcal{R}_{13} + \sin \mathcal{R}_{23}) - 2K_e + \mathcal{L}_3[V(d_3|1) - V(d_3|0)].$$

In the case of a long and posterior “nonroad” segment (with poor observation:  $V(d_3|0) = \log Z$  and  $\mathcal{L}_3 = 1$ ) and perfectly aligned segments, the following condition is deduced:  $K_e + K_{\mathcal{L}} < (-\log Z)/2$  (with  $\log Z < 0$ ). This choice is necessary to limit the connecting power of the *a priori* model in poor observation areas.

Secondly, comparing the energy of the “null configuration” with a road configuration energy [Fig. 15(b)], a relationship between the total length of the road and ( $K_i$ ,  $K_{\mathcal{L}}$ ) may be deduced. Indeed the energetic variation between both configurations is

$$\Delta U = 2K_e - 2K_{\mathcal{L}} \sum_{j=0}^n \mathcal{L}_j + K_c \left[ \sum_{j=0}^{n-1} \sin \mathcal{R}_{j(j+1)} \right] + \sum_{j=0}^n \mathcal{L}_j[V(d_j|1) - V(d_j|0)].$$

Choosing a road favorable situation (good observations,  $\forall i V(d_i|0) = 1 + \log Z$  and aligned segments), the energy of the corresponding configuration must be lower than the “null configuration” energy, implying the following condition:

$$2K_e - 2K_{\mathcal{L}} \sum_{j=0}^n \mathcal{L}_j - (1 + \log Z) \sum_{j=0}^n \mathcal{L}_j < 0.$$

Denoting the total length by  $\mathcal{L}_t$ , the following constraint is deduced:

$$\mathcal{L}_t > \frac{2K_e}{2K_{\mathcal{L}} + 1 + \log Z}.$$

The higher this ratio, the longer (or with higher measures) the detected roads.

The other parameters  $K_c$  and  $K_i$  have been chosen empirically. The higher  $K_c$  is, the straighter are the detected roads.  $K_i$  has been chosen to be of the same order as the other parameters.

Based on these remarks, some realizations are shown in Figs. 16 and 17 to illustrate the parameter influence on the obtained roads. The chosen test area is a part of the Aix-en-Provence, located in the South of France, image, where road detection is particularly difficult.

### C. Results on SAR Satellite Images

We illustrate the proposed method on real radar images showing the potential of the method and the difficulties remaining to solve. All the parameters are fixed once and for all for a single sensor since water channels appear with the same characteristics as the roads they are also detected.<sup>3</sup>

The first image [Fig. 18(a)] is a part of an ERS-1 PRI image of a very flat and rural area in The Netherlands. In this case, the line-detection step performs quite well [Fig. 18(b)], detecting most of the linear structures in the image. The connection step allows the recovery of the main road axes in the network and the channels [as can be seen comparing Fig. 18(c) and (d)]. On this sort of landscape, where roads are easily seen, most of the network can be detected.

The second ERS-1 image [Fig. 19(a)] is centered on the town Aix-en-Provence. In fact, most of the roads are hardly visible or not visible in this radar image, although an important road network covers this region [Fig. 19(d)]. Besides, difficulties occur in relief areas [right part of the image, Fig. 19(c)]. In this case, the line-detection step is clearly insufficient to give information on the linear structures [Fig. 19(b)]. The previously defined MRF is shown to be a powerful connection method, which is able to fill large gaps between the detected segments providing a map of the major roads, while suppressing most of the false-alarm detections [Fig. 19(c)]. In fact, the results are close to those which could be obtained by a human

<sup>3</sup>Other hydrological structures can be detected using more adapted *a priori* knowledge (especially on the curvature).

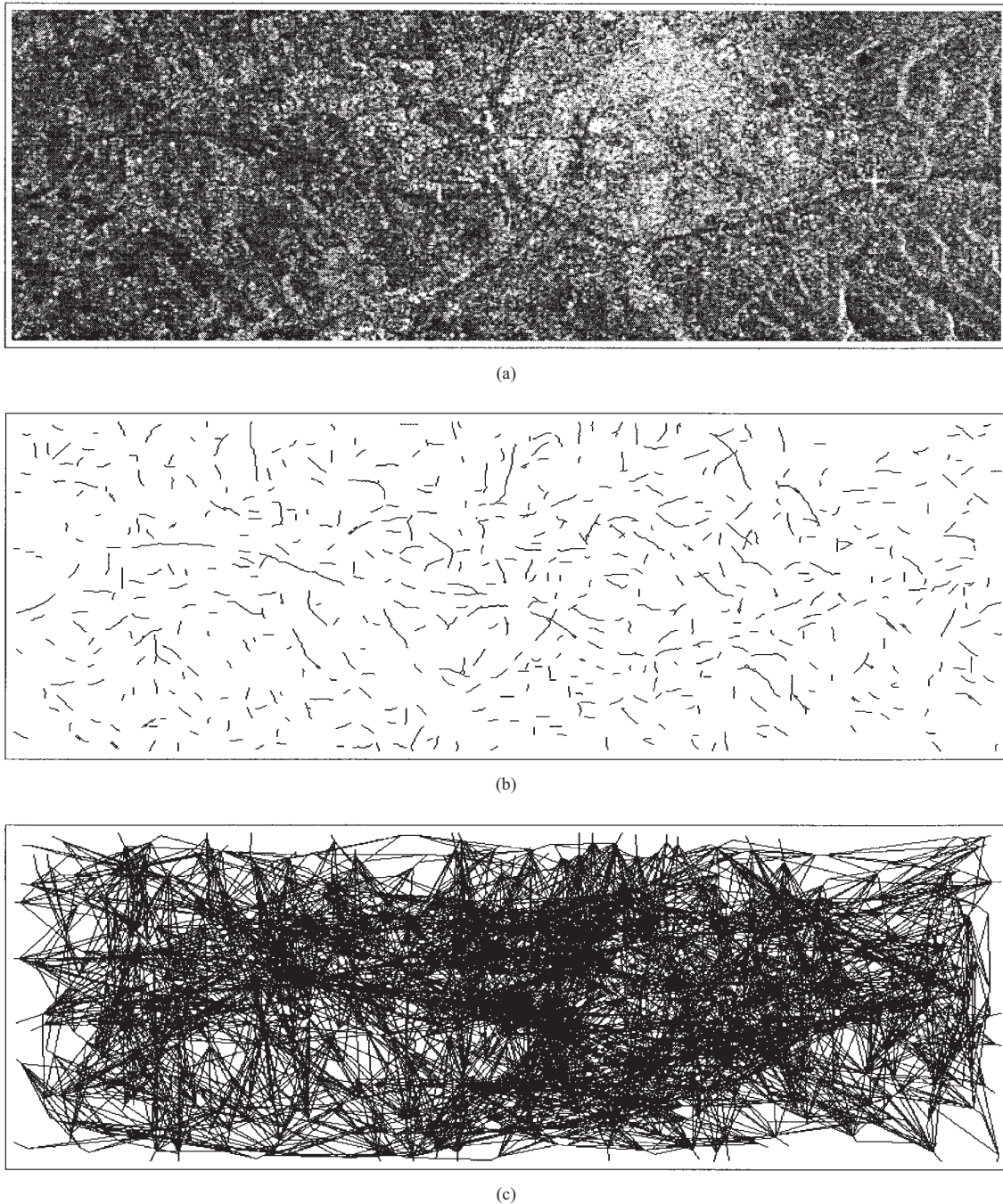


Fig. 16. Data used by the connection phase: original data, first step results, and the segment graph built. (a) Original ERS-1 image centered on Aix-en-Provence © ESA. Because the region is hilly, road detection is particularly difficult. (b) Segments obtained by the first local step of the method. Results are poor: many false detections and few segments on the real roads. (c) Graph segments: 839 segments have been detected after the first step, and with all the "possible" (with distance and angular constraints) connections, the graph contains 8891 segments.

observer without a map, and most of the main axes in the network are detected.

The third image is a SIR-C/X-SAR image of a region close from Strasbourg, France (Fig. 20). Since the number of looks is one, the parameter set for the line-detection step is more severe, whereas the same parameter set for *a priori* potentials has been kept. The line-detection step detects the

main axes, but results are noisy with many false alarms. Once again, the connection step is able to recover the main features (particularly a highway, a major road, and a channel). The last image is a RADARSAT image of Amsterdam, The Netherlands (Fig. 21). The parameter set for the line-detection and connection steps is the same as the one used for ERS-1 images. The same remarks as before can be made. Results are

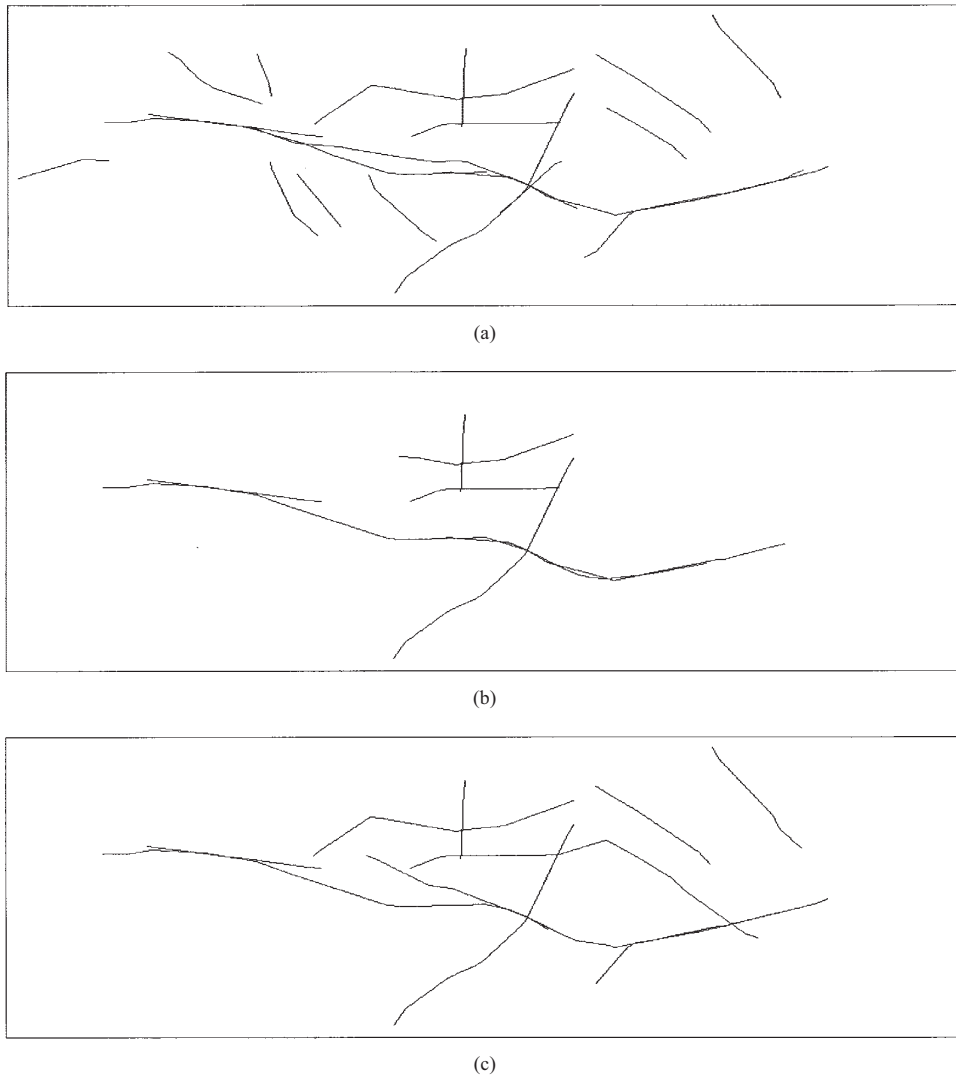


Fig. 17. Results of the Markovian connection scheme for different parameter sets.  $t_1$  and  $t_2$  are the thresholds defining the first-order potentials.  $K_e$ ,  $K_L$ ,  $K_i$ , and  $K_c$  are the parameters modeling an ideal road.  $K_e$  increasing and  $K_L$  decreasing lead to a decrease of the detected road number for fixed  $t_1$  and  $t_2$  [comparing (a) and (b)].  $t_2$  decreasing leads to more detected roads, as seen comparing (b) and (c). (a)  $t_1 = 0.2$ ,  $t_2 = 0.3$ ,  $\log Z = -0.65$ ,  $K_e = 0.1$ ,  $K_L = 0.2$ ,  $K_c = 0.3$ ,  $K_i = 0.2$ , and  $U = 0.53$ . (b)  $t_1 = 0.2$ ,  $t_2 = 0.3$ ,  $\log Z = -0.65$ ,  $K_e = 0.17$ ,  $K_L = 0.13$ ,  $K_c = 0.3$ ,  $K_i = 0.2$ , and  $U = 1.24$ . (c)  $t_1 = 0.2$ ,  $t_2 = 0.25$ ,  $\log Z = -0.67$ ,  $K_e = 0.17$ ,  $K_L = 0.13$ ,  $K_c = 0.3$ ,  $K_i = 0.2$ , and  $U = 2.06$ .

satisfying since the main axes are detected, but the detection is influenced by bright-point high density in the town, which increases false-alarm rates.

The whole method is rather demanding in computing time: for a  $1024 \times 1024$  image on a SPARC 10 processor, the line detection stage is about 10 min and the connection stage about 30 min for 20 000 segments (an ICM giving a local minimum takes 2 min).

## VI. CONCLUSION

In this paper, an almost unsupervised method has been proposed for detecting the main axes in road networks, as seen in satellite radar images. Our method includes both high- and low-level treatments.

The local line detectors deal with speckle images considering their statistical properties and having a constant false-alarm

rate, whatever the radiometry. Because they take into account both sides of the road, parts of the roads along dark fields or in dark areas, are not detected. Therefore, the quality of the detection, although higher than with concurrent methods, remains low, and a grouping step is necessary.

An original connection method has been developed, which is based on a MRF defined on a set of segments and takes into account the essential properties of a road network. This method has proven to be a powerful tool for connecting poor detection results, dealing with large gaps between segments and many false detections. The results obtained, although still insufficient in hilly areas, are good in flat areas.

In fact, the graph structure proposed is very general and could be adapted to other cases (hydrological or other linear structure detection).

Although the method is not entirely unsupervised, due to the setting of six parameters (two for the local line detectors and

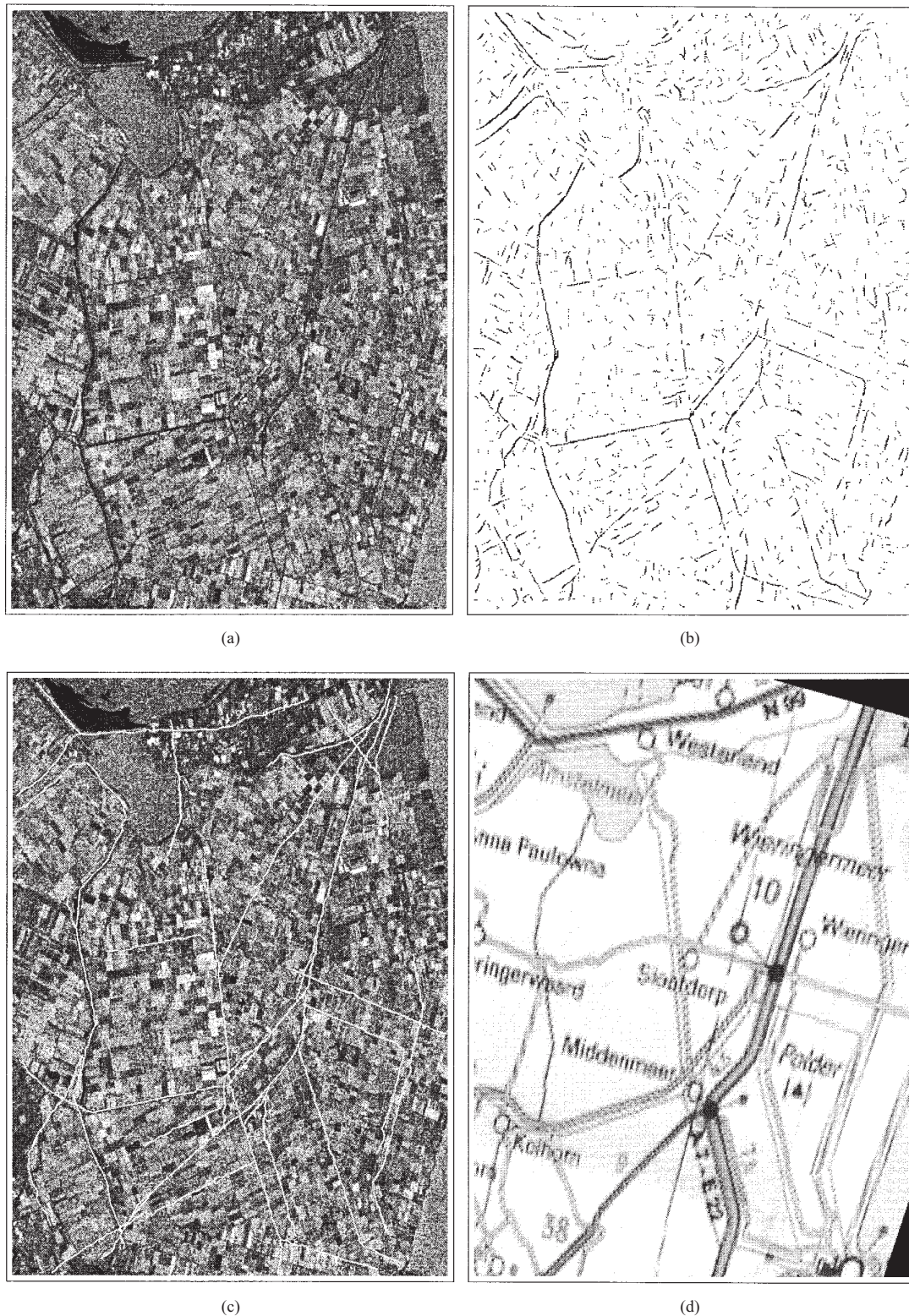


Fig. 18. Road detection process on a flat land. (a) Original ERS-1 image, part of an image of The Netherlands © ESA. The resolution is 25 m and the pixel spacing is 12.5 m with three looks. This is a flat and agricultural region with very well-defined fields. (b) Intermediate result: segments obtained after the first local step. On this flat land, enough segments are detected and the false detections are limited. (c) Final result of the road detection superimposed on the ERS-1 image. Almost all linear features (roads or channels) are detected. (d) Map corresponding to the image of North Holland © Michelin.

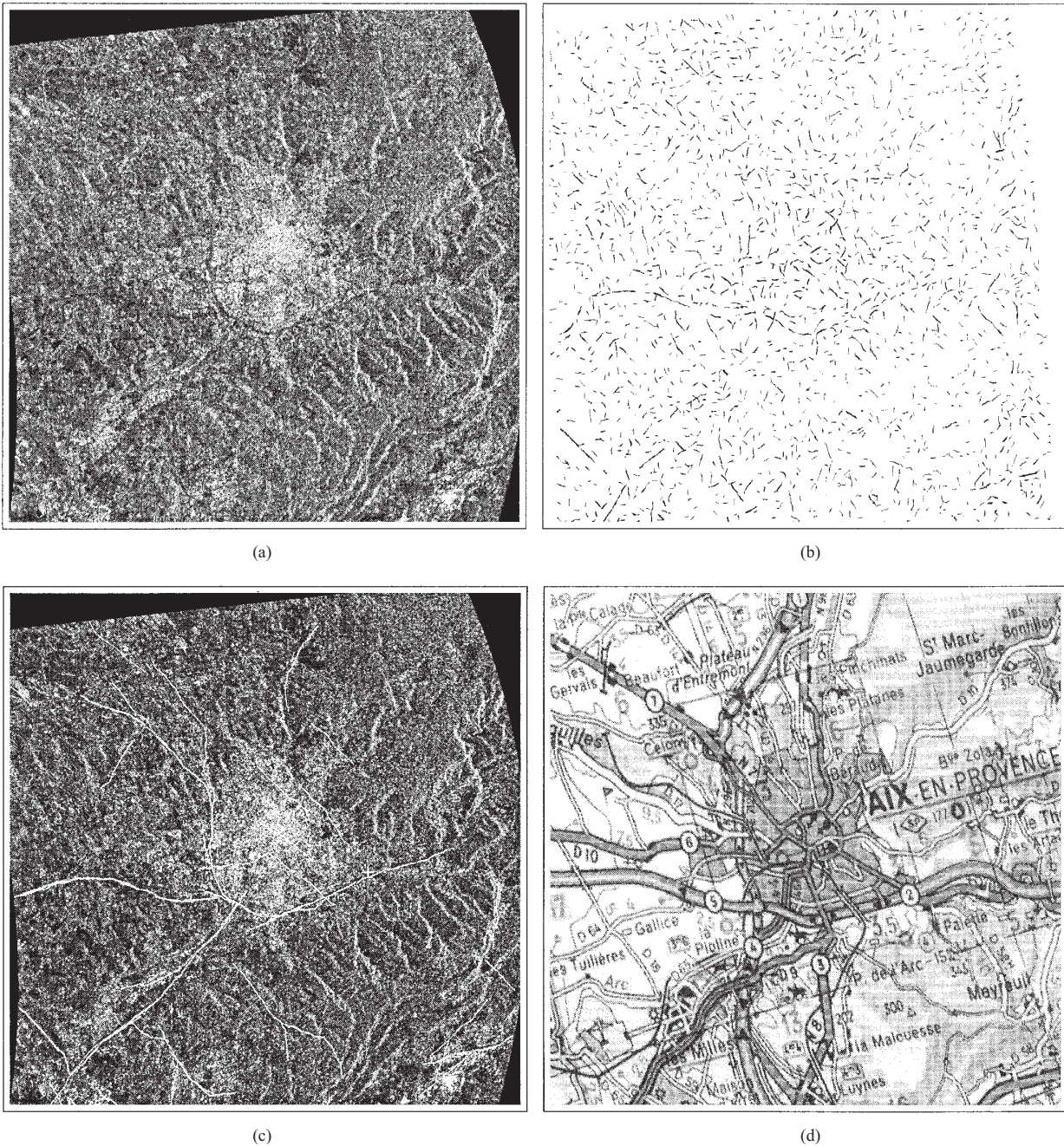


Fig. 19. Road detection process on a more hilly land (Aix-en-Provence, South of France). (a) Original ERS-1 image © ESA. This is a hilly region that is hard to interpret. Only the main axes of the road network are seen, although there are many roads on the scene. (b) Intermediate result: segments obtained after the first local step. On this hilly region, poor results are obtained: many “nonroad” segments are detected and few segments belonging to the true roads. (c) Final result of road detection superimposed on the ERS-1 image. Difficulties occur in relief areas (particularly the right part of the image). Only the main axes of the road network are detected. (d) Map corresponding to the image of Aix-en-Provence © Michelin.

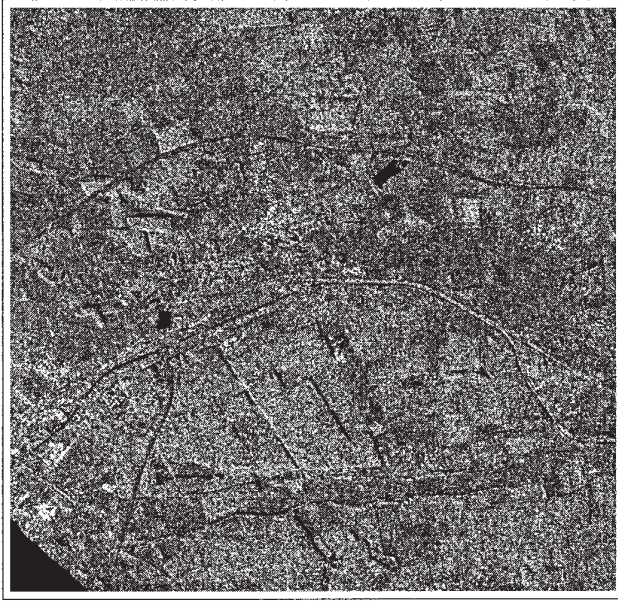
four for the connection method), we proposed for both steps a theoretical analysis to choose the parameters or to reduce the interval of choice.

One of the most important limitations of our method is the assumption that all roads may be found by connecting an initial detection with segments. Improvement could be obtained by looking for the best path between the extremities of the segments we try to connect. Further work includes also the

use of multitemporal filtered images and relief-effect-corrected images.

#### APPENDIX I

Let the amplitude empirical mean of region  $i$  computed on  $n_i$  pixels denote  $\mu_i = (1/n_i) \sum_{s \in i} A_s$ , and let the mean-reflected intensity denote  $\langle I_i \rangle$ . The  $\mu_i$  pdf corresponding to



(a)



(b)

Fig. 20. Road detection process on a SIR-C/X-SAR image. (a) Original SIR-C/X-SAR image © DLR/DFD. The resolution is 10 m and the pixel spacing is 6 m with one look. This is a flat land with some major roads and a channel (in the bottom of the image). (b) Result of road detection superimposed on the SIR-C/X-SAR image. The main axes of the road network and the channel are detected.

$n_i L$  equivalent looks is

$$f_{\mu_i}(t|\langle I_i \rangle) = \frac{2}{\Gamma(n_i L)} \left( \frac{n_i L}{\langle I_i \rangle} \right)^{n_i L} t^{2n_i L - 1} \cdot \exp\left(-\frac{t^2 n_i L}{\langle I_i \rangle}\right). \quad (7)$$

Let us note  $r^* = \mu_1/\mu_2$  and  $r_{12}^* = \min(\mu_1/\mu_2, \mu_2/\mu_1)$ . The  $r^*$  pdf is [27]

$$f_{r^*}(t|\langle I_1 \rangle, \langle I_2 \rangle) = \int_0^\infty f_{\mu_1}(tx|\langle I_1 \rangle) f_{\mu_2}(x|\langle I_2 \rangle) x dx \quad (8)$$

and using (7)

$$f_{r^*}(t|\langle I_1 \rangle, \langle I_2 \rangle) = \frac{4}{\Gamma(n_1 L)\Gamma(n_2 L)} \left( \frac{n_1 L}{\langle I_1 \rangle} \right)^{n_1 L} \left( \frac{n_2 L}{\langle I_2 \rangle} \right)^{n_2 L} \cdot t^{2n_1 L - 1} h(t|\langle I_1 \rangle, \langle I_2 \rangle)$$

where

$$h(t|\langle I_1 \rangle, \langle I_2 \rangle) = \int_0^\infty x^{2L(n_1+n_2)-1} \cdot \exp\left[-x^2\left(t^2 \frac{n_1 L}{\langle I_1 \rangle} + \frac{n_2 L}{\langle I_2 \rangle}\right)\right] dx.$$

Using a variable change,  $f_{r^*}(t|\langle I_1 \rangle, \langle I_2 \rangle)$  is deduced

$$f_{r^*}(t|\langle I_1 \rangle, \langle I_2 \rangle) = \frac{2\Gamma(n_1 L + n_2 L)}{\Gamma(n_1 L)\Gamma(n_2 L)} \left( \frac{n_1}{\langle I_1 \rangle} \right)^{n_1 L} \left( \frac{n_2}{\langle I_2 \rangle} \right)^{n_2 L} \cdot \frac{t^{2n_1 L - 1}}{\left(t^2 \frac{n_1}{\langle I_1 \rangle} + \frac{n_2}{\langle I_2 \rangle}\right)^{L(n_1+n_2)}}. \quad (9)$$

With the contrast between the radiometric means as  $c = \sqrt{\langle I_1 \rangle / \langle I_2 \rangle}$ , we have

$$f_r(t|c) = \frac{2\Gamma(n_1 L + n_2 L)}{\Gamma(n_1 L)\Gamma(n_2 L)} n_1^{n_1 L} n_2^{n_2 L} \cdot \frac{t^{2n_1 L - 1}}{\left(t^2 n_1 + n_2 c^2\right)^{L(n_1+n_2)}} c^{2n_2 L}. \quad (10)$$

Since for the random variable  $\min(x, y)$  the pdf is:

$$f_{\min(x, y)}(t) = f_x(t)\Phi_y(t) + f_y(t)\Phi_x(t)$$

$f_{r_{12}^*}$  is eventually obtained as

$$f_{r_{12}^*}(t|c) = \frac{2\Gamma(n_1 L + n_2 L)}{\Gamma(n_1 L)\Gamma(n_2 L)} n_1^{n_1 L} n_2^{n_2 L} \cdot \left[ \frac{c^{2n_2 L} t^{2n_1 L - 1}}{\left(t^2 n_1 + n_2 c^2\right)^{L(n_1+n_2)}} + \frac{\left(\frac{1}{c^2}\right)^{n_1 L} t^{2n_2 L - 1}}{\left(t^2 n_2 + \frac{n_1}{c^2}\right)^{L(n_1+n_2)}} \right]. \quad (11)$$

And defining  $r_{12} = 1 - r_{12}^*$ ,  $f_{r_{12}}(t|c) = f_{r_{12}^*}(1 - t|c)$ , and  $\Phi_{r_{12}}(t|c) = 1 - \Phi_{r_{12}^*}(t|c)$ .

Since  $r = \min(r_{12}, r_{13})$ , with  $c_{1i} = \sqrt{\langle I_1 \rangle / \langle I_i \rangle}$

$$f_r(t|c_{12}, c_{13}) = f_{r_{12}}(t|c_{12})\Phi_{r_{13}}(t|c_{13}) + f_{r_{13}}(t|c_{13})\Phi_{r_{12}}(t|c_{12}).$$



(a)



(b)

Fig. 21. Road detection process on a RADARSAT image. (a) Original RADARSAT image © Canadian Space Agency (available on the CD-ROM Radarsat International). The pixel spacing is 12.5 m with three looks. This is an image of the Amsterdam city (The Netherlands) with many roads and channels. (b) Result of road detection superimposed on the RADARSAT image. The main axes of the road network and hydrological linear structures are detected.

## APPENDIX II

Let us consider a fixed direction  $\mathbf{d}_k$  dividing the window  $V_{x_0}$  centered in  $x_0$  into two regions indexed by  $i$  and  $j$ . Noting  $A_s$  the amplitude random variable, and  $X_s$ , the random variable corresponding to the deduced edge population,  $\mu_A$ ,  $\mu_X$ ,  $\sigma_A$ , and  $\sigma_X$ , the empirical first-order statistics, mean and standard deviation computed on  $n$  pixels,  $A_s$  and  $X_s$ , the realizations of  $A$ , and  $X$  in pixel  $s$ , then  $\rho_{ij}$  is defined by

$$\rho_{ij} = \frac{1}{\sigma_A \sigma_X} \left( \frac{1}{n} \sum_{s \in i \cup j} A_s X_s - \mu_A \mu_X \right). \quad (12)$$

The following expression is deduced by using  $X$  values ( $X_s$  value is either  $\mu_i$  for a pixel belonging to region  $i$  or  $\mu_j$  for a pixel belonging to region  $j$ ,  $\mu_i$  and  $\mu_j$  being the empirical means of regions  $i$  and  $j$  computed on  $n_i$  and  $n_j$  pixels, with  $n = n_i + n_j$ )

$$\rho_{ij}^2 = \frac{\sigma_X^2}{\sigma_A^2}$$

and:

$$\sigma_X^2 = \frac{n_i n_j}{n^2} (\mu_i - \mu_j)^2$$

$$\sigma_A^2 = \frac{1}{n^2} [n_i n_j (\mu_i - \mu_j)^2 + n(n_i \sigma_i^2 + n_j \sigma_j^2)].$$

Let us remark that if we had chosen the unnormalized cross-correlation, the response would have been a generalized gradient not adapted to SAR images.

## ACKNOWLEDGMENT

The authors would like to thank the Russian Foundation of Fundamental Researches for its support and the reviewers for many helpful comments.

## REFERENCES

- [1] J. W. Goodman, "Statistical properties of laser speckle patterns," in *Laser Speckle and Related Phenomena*, vol. 9, J. C. Dainty, Ed. Heidelberg, Germany: Springer-Verlag, 1975, ch. 2, pp. 9–75.
- [2] C. J. Oliver, "The interpretation and simulation of clutter textures in coherent images," *Inverse Problems*, vol. 2, pp. 481–518, 1986.
- [3] D. M. McKeown and J. L. Denlinger, "Cooperative methods for road tracking in aerial imagery," in *Proc. IEEE Comput. Vision Pattern Recognit.*, Ann Arbor, MI, June 1988, pp. 662–672.
- [4] N. Merlet and J. Zerubia, "New prospects in line detection by dynamic programming," *IEEE Trans. Pattern Anal. Machine Intell.*, vol. 18, pp. 426–431, Apr. 1996.
- [5] D. Geman and B. Jedynek, "An active testing model for tracking roads in satellite images," *IEEE Trans. Pattern Anal. Machine Intell.*, vol. 18, pp. 1–14, Jan. 1996.
- [6] R. Welch and M. Ehlers, "Cartographic feature extraction with integrated SIR-B and Landsat TM images," *Int. J. Remote Sensing*, vol. 9, no. 5, pp. 873–889, 1988.
- [7] R. Samadani and J. F. Vesecky, "Finding curvilinear features in speckled images," *IEEE Trans. Geosci. Remote Sensing*, vol. 28, pp. 669–673, July 1990.
- [8] O. Hellwich, H. Mayer, and G. Winkler, "Detection of lines in synthetic aperture radar (SAR) scenes," in *Proc. Int. Archives Photogrammetry Remote Sensing (ISPRS)* vol. 31, Vienna, Austria, 1996, pp. 312–320.
- [9] G. J. Vanderbrug, "Line detection in satellite imagery," *IEEE Trans. Geosci. Electron.*, vol. GE-14, pp. 37–44, Jan. 1976.
- [10] M. A. Fischler, J. M. Tenenbaum, and H. C. Wolf, "Detection of roads and linear structures in low resolution aerial imagery using a multisource knowledge integration technique," *Comput. Graph. Image Processing*, vol. 15, no. 3, pp. 201–223, 1981.
- [11] J. Canny, "A computational approach to edge detection," *IEEE Trans. Pattern Anal. Machine Intell.*, vol. PAMI-8, pp. 679–698, Nov. 1986.
- [12] R. Touzi, A. Lopes, and P. Bousquet, "A statistical and geometrical edge detector for SAR images," *IEEE Trans. Geosci. Remote Sensing*, vol. 26, pp. 764–773, Nov. 1988.
- [13] M. Adair and B. Guindon, "Statistical edge detection operators for linear feature extraction in {SAR} images," *Can. J. Remote Sens.* vol. 16, no. 2, pp. 10–19, 1990.
- [14] C. J. Oliver, "Edge detection in SAR segmentation," in *Proc. EUROPTO, SAR Data Processing Remote Sens.*, vol. 2316, Rome, Italy, Sept. 1994, pp. 80–91.
- [15] J. W. Wood, "Line finding algorithms for SAR," in Royal Signals and Radar Establishment, Memo. 3841, 1985.
- [16] S. Quegan, A. Hendry, and J. Skingley, "Analysis of synthetic aperture radar images over land," in *Mathematics in Remote Sensing*. Danbury, 1986, pp. 365–379.
- [17] J. Skingley and A. J. Rye, "The Hough transform applied to {SAR} images for thin line detection," *Pattern Recognit. Lett.*, vol. 6, pp. 61–67, 1987.
- [18] P. Fua and Y. G. Leclerc, "Model driven edge detection," *Machine Vision Applicat.*, vol. 3, pp. 45–56, 1990.
- [19] C. S. Regazzoni, G. L. Foresti, and S. B. Serpico, "An adaptive probabilistic model for straight edge-extraction within a multilevel MRF framework," in *IGARSS'95*, Firenze, Italy, pp. 458–460.
- [20] A. Lopes, E. Nezry, R. Touzi, and H. Laur, "Structure detection, and statistical adaptive filtering in SAR images," *Int. J. Remote Sensing*, vol. 14, no. 9, pp. 1735–1758, 1993.
- [21] F. T. Ulaby, F. Kouyate, B. Brisco, and T. H. L. Williams, "Textural information in SAR images," *IEEE Trans. Geosci. Remote Sensing*, vol. GE-24, pp. 235–245, Mar. 1986.
- [22] A. Lopes, R. Touzi, and E. Nezry, "Adaptative speckle filters and scene heterogeneity," *IEEE Trans. Geosci. Remote Sensing*, vol. 28, pp. 992–1000, Nov. 1990.
- [23] F.-K. Li, C. Croft, and D. N. Held, "Comparison of several techniques to obtain multiple-look SAR imagery," *IEEE Trans. Geosci. Remote Sensing*, vol. GE-21, pp. 370–375, May 1983.
- [24] A. C. Bovik, "On detecting edges in speckle imagery," *IEEE Trans. Acoust., Speech, Signal Processing*, vol. ASSP-36, pp. 1618–1627, Oct. 1988.
- [25] M. Abramowitz and I. Stegun, *Handbook of Mathematical Functions*. New York: Dover, 1972.
- [26] E. Jakeman and J. A. Tough, "Generalized K distribution: A statistical model for weak scattering," *J. Opt. Soc. Amer.*, vol. 4, no. 9, pp. 1764–1772, 1987.
- [27] M. G. Kendall and A. Stuart, *The Advanced Theory of Statistics*, 3rd ed, vol. 1. London, U.K.: Griffin, 1969.
- [28] M. H. Hueckel, "An operator which locates edges in digitized pictures," *J. Assoc. Comput. Mach.*, vol. 18, pp. 191–203, Jan. 1971.
- [29] I. Bloch, "Information combination operators for data fusion: A comparative review with classification," *IEEE Trans. Syst., Man, Cybern.*, vol. 26, pp. 52–67, Jan. 1996.
- [30] R. D. Duda and P. E. Hart, "Use of the Hough transformation to detect lines and curves in pictures," *Commun. ACM*, vol. 15, no. 1, pp. 11–15, 1972.
- [31] E. S. Deutsch, "Thinning algorithms on rectangular, hexagonal, and triangular arrays," *Commun. ACM*, vol. 15, no. 9, pp. 827–837, 1972.
- [32] M. Kass, A. Witkin, and D. Terzopoulos, "Snakes: Active contours models," *Int. J. Comput. Vision*, vol. 1, no. 4, pp. 321–331, 1988.
- [33] D. G. Lowe, "Organization of smooth image curves at multiple scales," in *Proc. 2nd Int. Conf. Comput. Vision*, Orlando, FL, 1989, pp. 558–567.
- [34] C. David and S. W. Zucker, "Potentials, valleys and dynamic global coverings," *Int. J. Comput. Vision*, vol. 5, no. 3, pp. 219–238, 1990.
- [35] I. J. Cox, J. M. Rehg, and S. Hingorani, "A Bayesian multiple-hypothesis approach to edge grouping and contour segmentation," *Int. J. Comput. Vision*, vol. 11, no. 1, pp. 5–24, 1993.
- [36] J. L. Marroquin, "A Markovian random field of piecewise straight lines," *Biological Cybern.*, vol. 61, pp. 457–465, 1989.
- [37] S. Krishnamachari and R. Chellappa, "Delineating buildings by grouping lines with MRF's," *IEEE Trans. Image Processing*, vol. 5, pp. 164–168, Jan. 1996.
- [38] J. Besag, "Spatial interaction and the statistical analysis of lattice systems," *J. R. Statist. Soc. B*, vol. 36, pp. 192–326, 1974.
- [39] S. Geman and D. Geman, "Stochastic relaxation, Gibbs distribution, and the Bayesian restoration of images," *IEEE Trans. Pattern Anal. Machine Intell.*, vol. PAMI-6, pp. 721–741, Nov. 1984.
- [40] X. Descombes, J. F. Mangin, E. Pecharsky, and M. Sigelle, "Fine structures preserving Markov model for image processing," in *Proc. 9th Scandinavian Conf. Image Anal.*, Uppsala, Sweden, June 1995, vol. 2, pp. 349–356.



**Florence Tupin** received the engineer degree from École Nationale Supérieure des Télécommunications (ENST), Paris, France, in 1994.

She is currently a Ph.D. student at ENST in the Image Department. Her main research interests involve image analysis, Markovian random-field techniques, and SAR remote sensing.



**Jean-Marie Nicolas** graduated from École Normale Supérieure de Saint Cloud, Paris, France, in 1979 and received the Ph.D. degree in physics from the University of Paris XI, Paris, France, in 1982.

He was a Research Scientist at Laboratoire d'Electronique Philips (LEP) in medical imaging. He was then with Thomson CSF, working in signal and image processing. He is currently with École Nationale Supérieure des Télécommunications as an Associate Professor in the Image Department, and his main research interests concern radar imaging.



**Henri Maître** received the engineer degree from École Centrale Paris, Paris, France, in 1971 and the Dr.Sc. degree in physics from the University of Paris VI, Paris, France, in 1982.

He has taught digital picture processing at École Nationale Supérieure des Télécommunications (ENST), Paris, France, since 1973. As a Professor and Head of the Image Department at ENST, his research includes works on image analysis, image understanding, and computer vision.



**Eugène Pechersky** was born in 1937. He received a mathematics degree from Novosibirsk State University, Russia, in 1967 and the Ph.D. degree in mathematics from the Institute of Mathematics of the Siberian Branch of Academy of Science, Russia.

He works with the Institute for Problems of Information Transmission, Russian Academy of Science. His main scientific interests include Gibbs random fields and its applications to image processing and large deviation theory and its applications to queuing theory.



**Jean François Mangin** received the engineer degree from École Centrale Paris, Paris, France, in 1989, the M.Sc. degree in numerical analysis from University of Paris VI, Paris, France, in 1989, and the Ph.D. degree in signal and image processing from École Nationale Supérieure des Télécommunications (ENST), Paris, France, in 1995.

Since 1991, he has been with the Service Hospitalier Frédéric Joliot, Commissariat à l'Énergie Atomique, Orsay, France. His research interests include multimodal image registration, pattern recognition, image segmentation, mathematical morphology, Markovian random fields, deformable models, and brain functional mapping.